



Characteristics of strong ground motions and structural damage patterns from the February 6th, 2023 Kahramanmaraş earthquakes, Türkiye

Aybige Akinci¹ · Ahmet Anil Dindar² · Ihsan E. Bal³ · Deniz Ertuncay^{4,5} · Eleni Smyrou³ · Daniele Cheloni¹

Received: 23 January 2024 / Accepted: 30 July 2024
© The Author(s) 2024

Abstract

On February 6th, 2023, two severe earthquakes struck southeastern Türkiye near the Syrian border. The first earthquake, Mw7.8, occurred at 04:17 local time in the East Anatolian Fault Zone near the city of Gaziantep. The second earthquake, Mw7.5, occurred approximately 9 h later at 13:24 local time near Elbistan County, in Kahramanmaraş province. These seismic events ruptured multiple segments of the East Anatolian Fault Zone (EAFZ), with rupture lengths exceeding 300 km, and deformation exceeding 5 m on both sides of the faults. In this study, we aim to analyze characteristics of the strong ground motion induced by the mainshocks, focusing on ground motion intensity measures such as the peak ground acceleration (PGA), the peak ground velocity (PGV), and the pseudo-acceleration response spectra (PSA). The first earthquake produced extremely high PGA values in both horizontal (> 2 g) and vertical (> 1 g) components. At near field distances, large PGVs are measured (> 180 cm/s) with more than 30 impulsive motions which may indicate source-related effects. Large spectral demands are also recorded for both earthquakes, partially underestimated by Ground Motion Models (GMMs), especially in the near-field. Specifically, we compare the PSA for horizontal directions with the design spectra provided by both the new and previous Turkish building codes. We also present building and ground damage observations that provide insights into the observed ground motions in the heavily damaged areas.

Keywords Kahramanmaraş earthquakes · Ground motions · Pulse-like motion · Building damage · Seismic hazard

1 Introduction

The Kahramanmaraş earthquake sequence started on February 6th, 2023, at 04:17 local time (01:17:35 UTC) with an Mw7.8 earthquake near the Pazarçık district in Kahramanmaraş province (AFAD 2023a, b and United States Geological Survey, USGS 2023). According to the Kandilli Observatory and Earthquake Research Institute (KOERI), the epicenter was located at 37.11°N, 37.12°E (Fig. 1), originated on the Narlı Fault, and

Extended author information available on the last page of the article

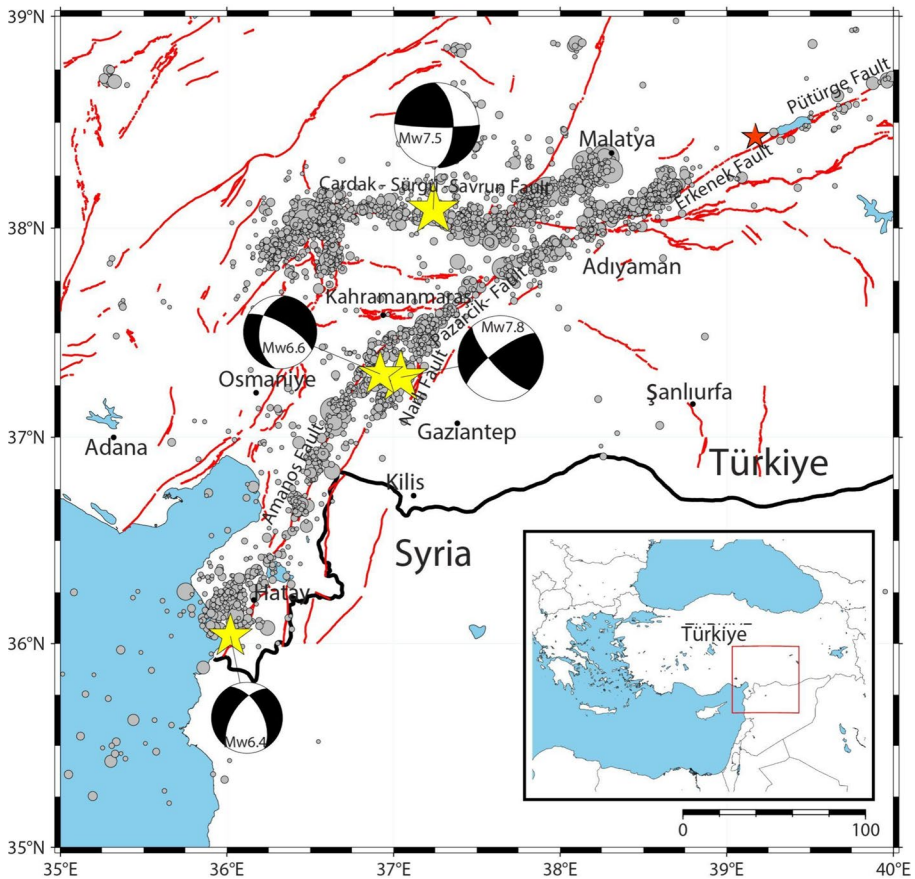


Fig. 1 A simplified map of the study area, showing the distribution of 6 months of aftershocks as provided by AFAD (AFAD, 2023a, b, c) related to the Mw7.8 and Mw7.5 earthquakes. The focal mechanisms of the earthquakes (yellow stars) with magnitudes greater than 6.0 are depicted on the map. The red lines displayed on the map represent the traces of known and mapped fault surfaces (Duman and Emre 2013). The circles represent the relocated aftershocks during the first 11 days after the main earthquakes. The size of each circle indicates the magnitude of the corresponding aftershock. Red stars present the Doğanyol-Elazığ 24 January 2020 M6.8 earthquake location. The black dots on the map indicate the locations of larger cities

propagated northward, rupturing various segments of the East Anatolian Fault (EAF). The spatial distribution of aftershocks reveals that the rupture extended as far south as Antakya-Hatay and terminated northeast near the Pütürge fault segment, close to the location of the previous 24 January 2020 Doğanyol-Elazığ earthquake sequence (Fig. 1). The total length of the rupture associated with the mainshock exceeded 300 km, resulting in significant surface displacement ranging from 3 to 5 m (Hancılar et al. 2023; Barbot et al. 2023; Melgar et al. 2023; Jia et al. 2023).

Approximately 9 h later, at 13:24 local time (10:24:48 UTC), the second earthquake, known as the Mw7.5 Elbistan earthquake, occurred, causing a surface rupture along the Çardak-Sürgü fault segment of the Northern Strand of the EAFZ and providing a remarkable example of short-term earthquake triggering. The epicenter of this earthquake

was determined to be located south of Elbistan with coordinates 38.07°N, 37.21°E (Fig. 1). The total length of the rupture associated with this second mainshock was approximately 160 km, with significant surface displacement observed in the 2–8-m range in the field (Cetin et al. 2023; Barbot et al. 2023; Melgar et al. 2023; Jia et al. 2023). Fault plane solutions for the main events (USGS 2023) indicated that both the Mw7.8 and Mw7.5 earthquakes agree with the activation of left-lateral strike-slip faults.

Based on historical earthquake records, these two segments have previously hosted a series of powerful earthquakes with magnitudes greater than 7.0. It is important to emphasize that prior to the recent seismic events, the region had a history of relatively low seismic activity despite the occurrence of significant historical earthquakes with magnitudes larger than 7.0 (Reilinger et al. 2006; Blettery et al. 2020). Çetin et al. (2023) have indicated that the apparent lack of recent seismic activity along the entire East Anatolian Fault Zone (EAFZ) may indicate that the fault is presently locked. In fact, the area remained relatively seismically quiescent for many centuries (Ambraseys 1989; Nalbant et al. 2002) and the earthquakes on February 6th occurred within a seismic gap marked by low geodetic strain rates where deformation is dispersed across a broad fault zone with a substantial time interval between historical events (Bulut et al. 2012).

Following the earthquakes on February 6th, 2023, a total of 28,990 aftershocks with a magnitude larger than two were recorded, with a total of 13 above magnitude 5.5 (as of May 29, 2023, according to AFAD, 2023a, b, c). Figure 1 illustrates the distribution of aftershocks in the sequence, emphasizing the most significant events with magnitudes greater than 6.0. These relatively larger magnitude events ($M > 6.0$) occurred on February 6th, approximately ten minutes after the mainshock, with a M6.7 event, located 14 km east of Nurdağ, and ten hours later a M6.0 earthquake occurred 4 km northeast of Göksun. Another noteworthy event occurred two weeks later, on February 20th, towards the southwestern termination of the mainshock rupture, near Antakya, with an event of M6.4.

The strong motion recordings from the initial mainshock revealed peak ground accelerations reaching up to 1.0 g in locations near the fault rupture (Hu et al. 2024). These acceleration levels indicate extremely intense shaking, resulting in severe structural damage (Demir et al. 2024). Subsequently, the ground motion generated by the second mainshock has further impacted structures already weakened by the first event, possibly increasing the extent of damage and destruction. As of May 2023, the earthquakes have tragically resulted in over 55,000 reported fatalities, along with numerous injuries and the displacement of more than 1.5 million individuals (Ministry of Environment, Urbanization and Climate Change, 2023). The provinces most significantly affected by the seismic activity, including Hatay, Kahramanmaraş, Gaziantep, Malatya, and Adıyaman, have sustained substantial damage to both buildings and infrastructure. Collectively, these provinces account for 81% of the estimated damage and are home to approximately 6.45 million people, representing around 7.4% of the total population of Türkiye (GRADE Report 2023). Our study contributes to the understanding of seismic characteristics and strong motion patterns, conducting detailed investigations into the destruction pattern, factors, and seismogenic mechanisms of this specific earthquake doublet. The Mw7.8 earthquake is the largest in Türkiye since the 1939 Erzincan earthquake of the same magnitude. It resulted in severe losses, with more than 55 thousands victims and extensive damages, rendering more than 18,000 buildings unusable in the epicentral area. The presence of numerous aftershocks, some with magnitudes exceeding 5.0, heightened the risk of collapse for structures already partially damaged by the mainshock.

After the seismic events, numerous researchers have examined the effects and features of the earthquakes, resulting in a large number of scientific studies being published in a

short period of time. These studies mostly focus on various aspects of the sequence, ranging from kinematic to dynamic source rupture characteristics, seismic activity aftershock distribution, and ground motion characteristics of the earthquake doublet, from a seismological perspective and/or solely from an engineering standpoint (Ren et al. 2024; Wang et al. 2023; Ding et al. 2023; Cetin et al. 2024). However, our study offers an overarching perspective encompassing both the ground motion characteristics and providing insights into its potential impact on the observed damages across the study area. This paper focuses on analyzing strong ground motion generated by the mainshocks, employing accelerometric data. The aim is to investigate the characteristics of ground motion, with a specific focus on engineering-relevant parameters. This includes ground motion intensity measures such as the peak ground acceleration (PGA), the peak ground velocity (PGV), and the pseudo-acceleration response spectra (PSA), as well as their variability over the study region. Subsequently, the recorded ground motions with predictions from selected ground motion models (GMMs), which play a central role in seismic hazard analysis, are compared (Gülerce et al. 2023). In addition, the observed horizontal and vertical PSA are compared to the design spectrum outlined in the current and previous Turkish building codes (TBDY, 2018 and TBEC 2007, hereafter TBDY 2018 and TBEC 2007). The present study also investigates earthquake source-related effects, focusing on impulsive signals and their presence in near-fault regions. Connections between the widespread damage sustained by reinforced concrete buildings and the observed effects related to both current and past Turkish seismic design codes are also discussed.

2 Seismotectonic setting and seismicity of the region

The seismic hazard in Türkiye is primarily driven by two major fault systems: the North Anatolian Fault Zone (NAFZ) and the EAFZ (McKenzie 1972; Taymaz et al. 2004). The EAFZ is a complex fault zone characterized by left-lateral strike-slip motion. Extending approximately 450 km from Karlıova to Hatay (Fig. 1), it serves as the boundary between the Anatolian Plate and the northern region of the Arabian Plate (Ambraseys 1989; Ambraseys and Jackson 1998; Duman and Emre 2013). This results in a left-lateral slip rate of about 10 mm/yr along the EAFZ (Reilinger et al. 2006). The cumulative displacement along the EAFZ is estimated to range from 15 to 30 km (Şaroğlu et al. 1992). Various authors have proposed its division into multiple fault segments. In accordance with Duman and Emre (2013), the fault segments along the primary trace of the EAFZ from southwest to northeast are delineated as the Amanos, Pazarcık, Erkenek, Pütürge, Palu, Illica, and Karlıova segments (refer to Fig. 2 in Duman and Emre 2013). The fault segments' lengths vary between 30 and 100 km. The EAFZ also demonstrates different strike-slip rates across its segments: 10–13 mm/yr on the Pütürge-Palu segment, 4–7 mm/yr on the Pazarcık-Erkenek segment, and 1–3 mm/yr on the Amanos segment. These values are derived from geological studies (e.g., Allen et al. 2004; Westaway 2004; Duman and Emre 2013) and geodetic measurements (e.g., Reilinger et al. 2006; Walters et al. 2017; Aktug et al. 2016; Bletery et al. 2020). While this region has been historically characterized by high seismic activity, including a series of significant surface-rupturing earthquakes in centuries past along the EAFZ (such as the 521 M7.5, the 1513 M7.4, and the 1893 M7.2), recent decades have seen a decrease in seismic activity along the EAFZ (Ambraseys 1989, 2009; Hubert-Ferrari

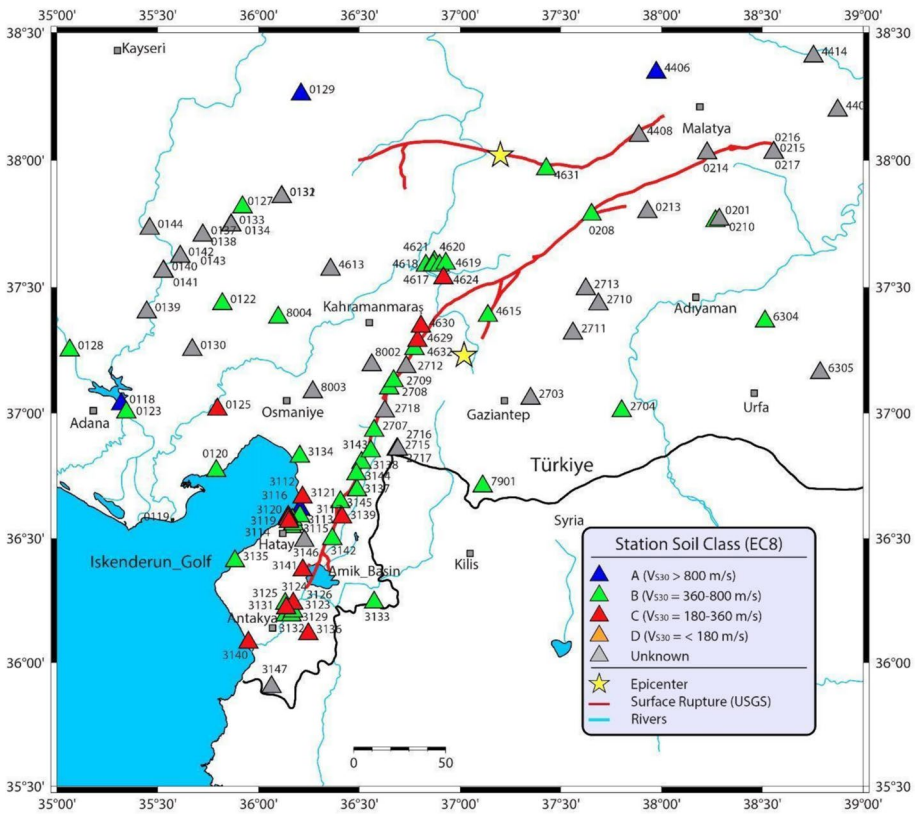


Fig. 2 Distribution of strong-motion stations belonging to the AFAD network, marked by triangles. Symbol color is related to site classification according to NTC-18 based on the parameter. The red lines displayed on the map represent the fault rupture of the Kahramanmaraş, Türkiye, Earthquake Sequence on February 6th, 2023, as produced by USGS

et al. 2020; Sbeinati et al. 2005; Sesetyan et al. 2013, 2020). In contrast, the NAFZ has been responsible for numerous earthquakes throughout the twentieth century, leading to its more extensive examination in research studies. Nevertheless, some studies have emphasized how this extended period of seismic quiescence may serve as a precursor for future seismic events (e.g., Nalbant et al. 2002; Duman and Emre 2013; Karabacak and Altunel 2013). In particular, before the February 6th, 2023 Kahramanmaraş earthquake sequence, multiple studies identified important seismic gaps along both the main and the northern strand of the EAFZ (e.g., Duman and Emre 2013; Aktug et al. 2016; Bulut et al. 2012) such as the Pazarcik, the Amanos and the Pütürge segments of the main strand, and the Çardak-Sürgü-Savrun segments of the northern strand. Following the Mw6.8 Doğanyol-Elazığ Earthquake sequence in 2020, affecting a part of the Pütürge segment, numerous investigations have extensively examined the true seismic potential of the EAFZ (e.g., Cheloni and Akinci 2020; Ragon et al. 2021; Tatar et al. 2020).

3 Observed strong ground motion from near-fault records

The Mw7.8 Pazarçık and Mw7.5 Elbistan earthquakes were recorded at 134 and 108 AFAD strong-motion stations, respectively, within a 250 km distance of the fault rupture. The AFAD stations are well-documented and provide extensive information, most of the time including the V_{s30} parameter (the average shear wave velocity in the top 30 m of soil at each station). They also offer fundamental resonant frequencies and corresponding soil types according to European Seismic Design Codes (EC8, CEN 2004). For the first event, information on the V_{s30} was available for 103 stations, and for the second event, it was available for 81 stations. V_{s30} information for other stations is retrieved using the model developed by Okay and Özacar (2023). Figure 2 displays the distribution of the strong-motion stations as a function of station soil class (European Seismic Design Codes, EC8, (CEN 2004) together with the V_{s30} for the recordings from the first and second events.

In this study we first process the strong-motion data following a series of analyses to ensure its relevance to the outcomes (Boore et al. 2012; Boore and Bommer 2005). The processing included the following steps: i) detrending, ii) 4th-order Butterworth filtering between 0.02 Hz and 50 Hz, which were appropriately padded with zeros to mitigate filter transient effects at both the beginning and end of the record, and iii) tapering. Furthermore, the waveforms were visually inspected, and any data with issues, such as significant gaps in the trace, were removed from the database. The raw data were processed homogeneously. Moreover, alternative procedures for the automated process of filtering, normalizing, and creating databases for big data are available (Abbaszadeh Shahri et al. 2024).

In Fig. 3, the distribution of the accelerometric time histories recorded at 20 selected strong-motion stations, situated approximately 20 km both east and west of the fault rupture trace (Reitman et al. 2023), are presented. The time histories are depicted as a move-out plot, illustrating the two horizontal components (North–South, NS, and East–West, EW) along with the vertical component (Up–Down). This representation encompasses all processed acceleration records within a 250 km epicentral distance from the Mw7.8 mainshock.

The recorded time histories at stations in close proximity to the epicenter clearly depict discernible rupture episodes. Stations 2709, 2712, and 4615, located approximately 21 km from the epicenter both north and south of the nucleation point, reveal such distinct episodes associated with the Mw7.8 earthquake. In contrast, at stations farther away from the epicenter, such as the 3145 and 3146 sites, these rupture episodes become indistinguishable.

The severity of ground motions is apparent when observing the high PGA values, especially at stations 4614, 2708, 3125, 3126, and 3129. In particular, station 4614 recorded PGAs of 3066 cm/s^2 and 2212 cm/s^2 on the EW and NS horizontal components, respectively. Stations 2708 and 3129 recorded 2191 cm/s^2 and 1361 cm/s^2 on the NS horizontal components during the earthquake. In comparison, stations 4614, 3125, and 3117 recorded PGA values as high as 2057 cm/s^2 , 1233 cm/s^2 , and 1151 cm/s^2 on the vertical component, respectively. Interestingly, three out of four stations—3125 (soil site class C), 3126 (class D), and 3129 (class C)—were located in the Antakya-Hatay area situated at the southern end of the fault rupture, 200 km far from the epicenter. Table 1 and Table 2 provide a comprehensive overview of the peak values recorded at each station, encompassing critical parameters such as PGA, PGV, and spectral acceleration for the two horizontal and the vertical components for the Pazarçık and Elbistan earthquakes, respectively. The largest PGVs are recorded at stations 3138, 3139, and 3123 with values

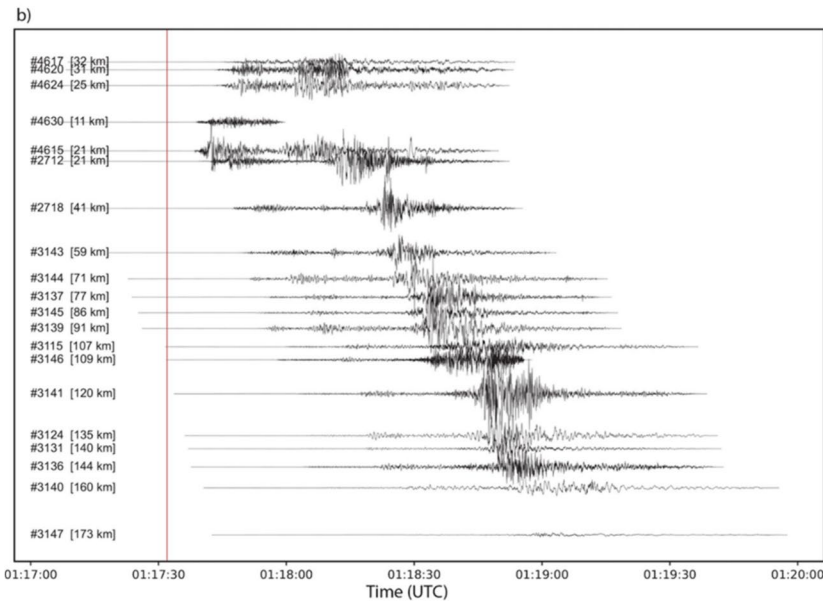
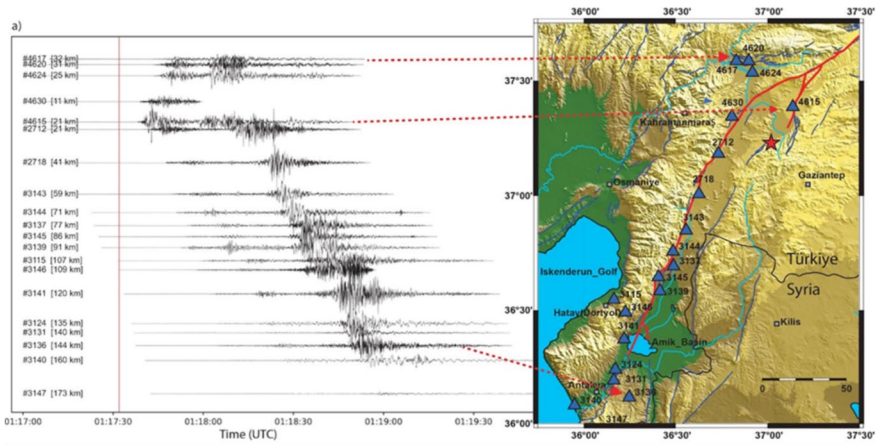


Fig. 3 Moveout plot for all processed acceleration records (up to 250 km epicentral distance) from the Mw7.8 mainshock. The horizontal components East–West, EW (a), North–South, NS (b), and the vertical, UP (c) components are shown for all records. Red horizontal line represents the origin time of the event in UTC. The red lines on the map depict the fault rupture associated with the Kahramanmaraş, Türkiye, Earthquake Sequence on February 6th, 2023, as reported by USGS

of 218.4 cm/s, 181.8 cm/s, and 164.5 cm/s, while many other stations exhibit PGVs of around 100 cm/s. However, unexpectedly high PGA (1409 cm/s²) and PGV (108.6 cm/s) values in the vertical component at station 3138 can be observed due to the momentary bounce of the site (Goto et al. 2019, Fig. S1).

Permanent displacements have also been calculated for some selected recordings that exhibited large accelerations. Figure 4 showcases the corrected acceleration, velocity, and

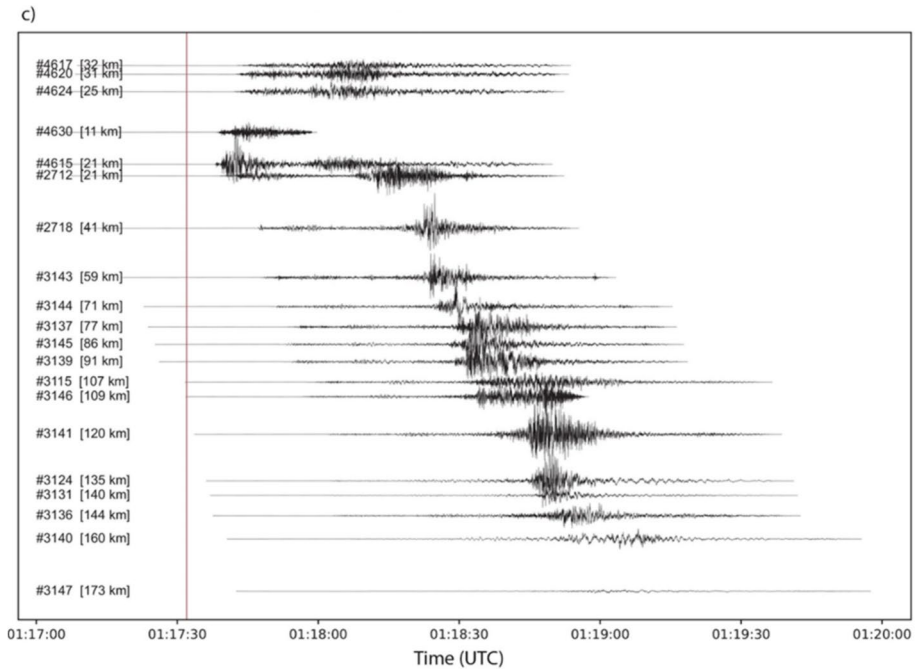


Fig. 3 (continued)

displacement traces of the main shock for stations 4615, 4624, 2712, 2718, 3144, and 3139. The calculated PGDs at these stations are around 1.5–2.0 m for stations 4615, 2718, 3144, and 3139, and around 1.0 m for stations 4624 and 2712. These permanent displacements are generally consistent with the displacements obtained from geodetic (InSAR and GNSS) data (Barbot et al. 2023; Cheloni et al. 2024) and from field observations (Meng et al. 2024; Yang et al. 2024).

The time histories, including acceleration, velocity, and displacement, for the stations located in Antakya-Hatay from a small local network, are also presented in Fig. 5. One of the earthquake's highest PGA values was recorded in Hatay at station 3129 with 1361 cm/s^2 , in the NS component. The PGV values were also high at these stations, being 181.8 cm/s and 163 cm/s at stations 3123 and 3129, and around 100 cm/s for most of the remaining stations. Remarkably, spectral acceleration exhibits exceptionally high values in the low-period range (PSA at 0.2 s) for the ground motion recorded at stations 3126 and 3129, being 5095 cm/s^2 and 4457 cm/s^2 , respectively. In contrast, station 3131, located on class B sites, recorded a PGA value of 373.2 cm/s^2 and a PGV value of 48.4 cm/s during the Mw7.8 event. In this study, we did not explore the influence of site amplification on ground motion, a topic that warrants investigation, especially in the Antakya area with the presence of the Amik basin and surrounding high mountainous areas (Fig. 5). This aspect will be the focal point of our upcoming studies, aligning with our primary objectives.

Table 1 GMPs of stations with less than 30 km of R_{jb} distance in the Pazarcık earthquake. Channel-based GMPs are given only for PGA for the sake of simplicity. In Table S1, channel-based GMPs are given for all parameters. * Station 213 does not record the entire earthquake; however, it manages to capture the impulsive motion

Station	R_{jb} (km)	PGA (cm/s ²)			PGV (cm/s)	PSA (T=0.2 s, cm/s ²)	PSA (T=1.0 s, cm/s ²)	PSA (T=2.0 s, cm/s ²)
		EW	NS	Z				
201	23.75	228.93	189.05	225.37	21.79	495.39	83.75	65.33
213*	4.52	169.99	240.27	300.94	100.45	568.31	372.04	473.14
2708	1.36	1193.57	2191.35	812.52	127	1533.97	1206.44	789.27
2712	0.00	621.76	566.92	366.49	93.89	1743.29	1429.21	460.84
2718	0.00	662.37	707.79	586.69	126.72	1632.15	870.45	413.87
3112	20.62	72.82	61.26	84.77	10.22	167.49	168.53	60.59
3115	16.65	230.07	289.01	210.29	53.06	858.85	361	293.85
3116	16.55	172.32	168	157.36	43.05	570.09	285.57	163.5
3117	16.28	991.38	1135.61	1151.4	149.65	1358.4	519.68	395.99
3123	0.00	602.51	635.8	847.59	181.82	1530.65	1751.85	1052.12
3124	0.00	640.82	570.67	578.68	115.25	1383.97	2039.03	814.18
3125	2.37	1126.75	829.19	1233.09	99.51	1704.49	570.2	410.68
3126	0.90	1017.09	1195.23	1085.13	103.92	5095.44	1048.98	717.06
3129	0.00	1209.74	1361.88	799.52	163.03	4457.4	1902.96	781.14
3131	0.00	373.19	368.74	154.53	48.39	631.55	729.68	351.11
3132	0.00	520.13	528.92	352.98	63.58	1267.77	1068.22	423.62
3133	28.78	144.36	217.68	87.68	34.12	300.41	415.5	190.27
3134	28.61	205.15	247.4	139.92	43.7	563.19	450.05	208.57
3136	4.64	397.17	530.89	223.57	55.74	1238.48	522.55	328.02
3137	0.00	838.26	460.67	485.83	107.27	1447.07	579.53	418.01
3138	0.00	734.21	904.93	1408.7	218.4	1528.54	2216.73	802.55
3139	0.00	492.04	569.11	368.02	164.48	1164.99	1159.36	1088.92
3140	13.53	211.78	191.01	175.11	67.99	441.73	677.27	396.86
3141	1.58	880.09	928.78	896.83	111.66	2148.26	928.78	705.53
3142	0.00	766.22	660.47	514.52	86.67	1419.05	624.67	265.81
3143	0.00	365.06	392.16	410.46	105.2	1416.96	845	479.34
3144	0.00	743.35	600.67	445.91	127.16	964.33	716.06	523.49
3145	0.00	729.37	600.74	619.64	146.03	1495.09	1403.47	470.34
3146	7.54	332.66	485.95	312.08	52.91	871.68	384.72	180.22
4404	20.85	141.32	134.51	93.82	25.19	285.78	160.11	54.36
4408	24.51	137.81	104.41	95.5	30.41	313.92	191.75	145.57
4611	17.14	320.58	353.39	169.43	50.43	875.43	373.94	199.23
4614	6.77	3066.13	2211.55	2057.68	77.6	4781.09	494.55	267.7
4615	0.00	547.41	562.84	675.06	135.21	1609.08	1056.71	564.13
4616	1.48	460.73	647.91	385.61	77.18	1445.16	589.15	280.58
4617	21.81	106.92	141.93	112.49	29.92	450.9	148.21	137.11
4618	21.34	153.4	125.11	138.13	28.56	420.19	157.44	98.07
4619	20.30	190.97	305.15	178.95	35.69	762.18	256.76	135.15
4620	18.67	319.19	293.92	188.23	42.96	1120.8	172.99	126.18
4621	18.04	289.04	367.42	238.6	45.6	644.49	322.74	269.14

Table 1 (continued)

Station	R_{jb} (km)	PGA (cm/s ²)			PGV (cm/s)	PSA (T=0.2 s, cm/s ²)	PSA (T=1.0 s, cm/s ²)	PSA (T=2.0 s, cm/s ²)
		EW	NS	Z				
4624	12.77	320.5	369.07	164.06	55.27	829.72	793.45	246.03
4625	10.06	486.08	455.91	368.84	64.19	1827.84	649.34	377.17
4626	16.86	124.75	112.18	102.5	25.1	210.26	112.61	44.23
8002	14.84	196.03	255.74	331.68	43.88	516.32	567.13	184.75
KHMN	0.00	423.21	514.94	418.74	93.37	1200.85	528.71	357.66
NAR	0.00	560.51	753.96	484.98	102.94	1207.11	616.62	404.53

Table 2 GMPs of stations at less than 50 km R_{jb} distance from the Elbistan earthquake. In Table S2, channel-based GMPs are given for all parameters

Station	R_{jb} (km)	PGA (cm/s ²)			PGV (cm/s)	PSA(T=0.2 s, cm/s ²)	PSA(T=1.0 s, cm/s ²)	PSA(T=2.0 s, cm/s ²)
		EW	NS	Z				
127	45.17	59.95	51.09	35.65	19.8	160.53	58.95	44.73
129	32.41	171.59	155.54	86.37	16.12	333.91	71.64	43.48
131	23.6	345.73	418.95	83.99	22.54	1674.76	82.65	42.64
132	23.68	60.67	62.48	56.96	19.77	211.87	68.68	42.63
213	27.13	127.78	125.19	71.43	25.4	265.73	252.79	194.14
4406	21.65	394.53	480.27	299.83	35.26	658.58	362.35	114.54
4412	37.57	125.93	151.98	83.46	35.53	278.38	319.21	165.28
4414	45.68	63.35	52.68	37.39	5.19	114.78	27.76	12.95
4611	28.19	139.52	197.16	72.48	32.52	463.39	224.71	89.35
4612	0	522.06	642.59	443.95	164.34	876.63	716.77	677.74
4613	41.77	76.72	72.48	77.45	19.14	157.74	105	69.24
4620	49.63	78.36	68.39	55.13	31.83	140.54	96.35	124.38

4 Comparison with ground motion models

In this section, we compare the observed and predicted ground motions for the Pazarcık and Elbistan earthquakes using several ground motion parameters, including PGA, PGV, PSA (T=0.2 s), PSA (T=1.0 s), and PSA (T=2.0 s). The predictions were obtained from GMMs developed by Boore et al. (2014) (hereafter **BSSA14**) and Kale et al. (2015) (hereafter **KALE15**). The **KALE15** model is based on a dataset obtained from the Earthquake Model of the Middle East Region (EMME) (Akkar et al. 2014). This dataset consists of over 650 accelerometric waveforms from 175 earthquakes with Joyner-Boore (R_{jb}) distances of 200 km or less. Earthquakes in the database had a maximum magnitude of 7.6, occurring in Türkiye and its surrounding regions. On the other hand, **BSSA14** is based on a global database obtained from NGA-West2 (Ancheta et al. 2014). This database comprises more than 20,000 waveforms recorded at R_{jb} distances of 1600 km or less from 599 earthquakes, with a maximum magnitude of 7.9.

In Fig. 6, we provide a comparison of observed and predicted ground motion intensity measures for the Pazarcık and Elbistan earthquakes as a function of the R_{jb}

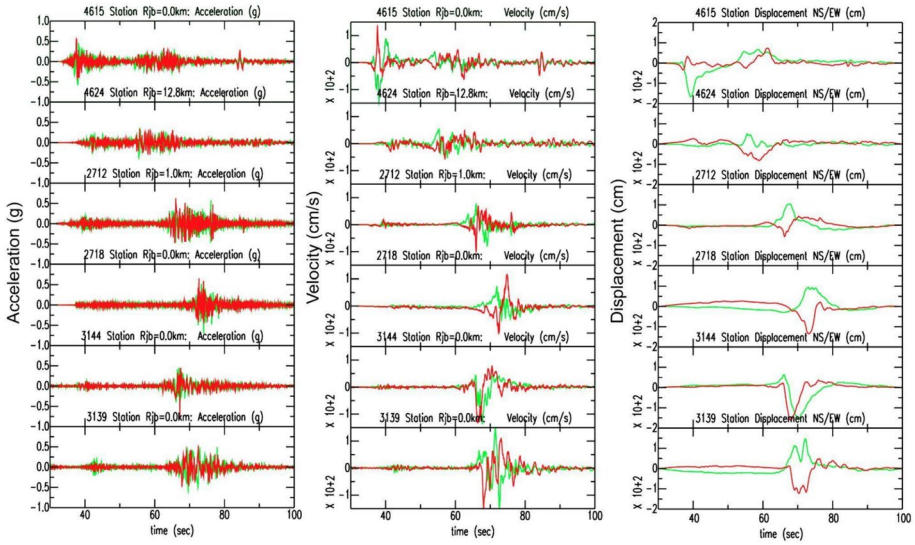


Fig. 4 Time series of the strong ground motions as the processed recorded acceleration, computed velocity, and computed displacement for the two horizontal components (EW-red and NS-green) at stations located over the fault rupture; Stations located from north to the south, 4615, 4624, 2712, 2718, 3144, 3139 of the Mw7.8 event

distances, calculated using the simplified planar faults developed by USGS (2023a, 2023b). Most horizontal PGAs for both earthquakes generally fall within the expected range defined by the **BSSA14** and **KALE15** models, although some exceptions exist. For the Pazarcık Mw 7.8 earthquake in particular, we observe several stations where the recorded PGA values significantly exceeded the predictions provided by the GMMs. We noticed that the **KALE15** model predicts lower PGA values compared to the **BSSA14** model. A similar pattern was observed in the comparison between observed and predicted PGA values for the Elbistan Mw7.5 earthquake. The **BSSA14** model exhibited slightly better accuracy in predicting the observed PGAs with relatively small differences than **KALE15**. Up to distances of 150 km, both models displayed a similar trend with respect to distance, while the **BSSA14** model showed stronger attenuation at longer distances.

However, the analysis of PGVs reveals an interesting pattern, as both GMMs consistently underestimate the observed peak ground velocities. For the Pazarcık earthquake, this underestimation is particularly evident for stations located between 10 and 200 km R_{jb} distances. Stations near the fault plane ($R_{jb} < 5$ km) show a mix of well-predicted and under-predicted PGVs. In contrast, for the Elbistan earthquake, a significant number of PGV observations exceed the predictions of the GMMs. This observation raises the possibility of an earthquake rupture directivity effect, a phenomenon where seismic waves are concentrated in a specific direction, resulting in higher velocities (Bray and Rodriguez-Marek 2004; Mavroeidis and Papageorgiou 2010).

The pseudo-spectral acceleration at different periods, specifically PSA ($T=0.2$ s), PSA ($T=1.0$ s), and PSA ($T=2.0$ s), are selected as they provide an indication of seismic loads for buildings of different sizes. In both earthquakes, a consistent trend is observed, with larger ground accelerations recorded as the period increases, in comparison to the

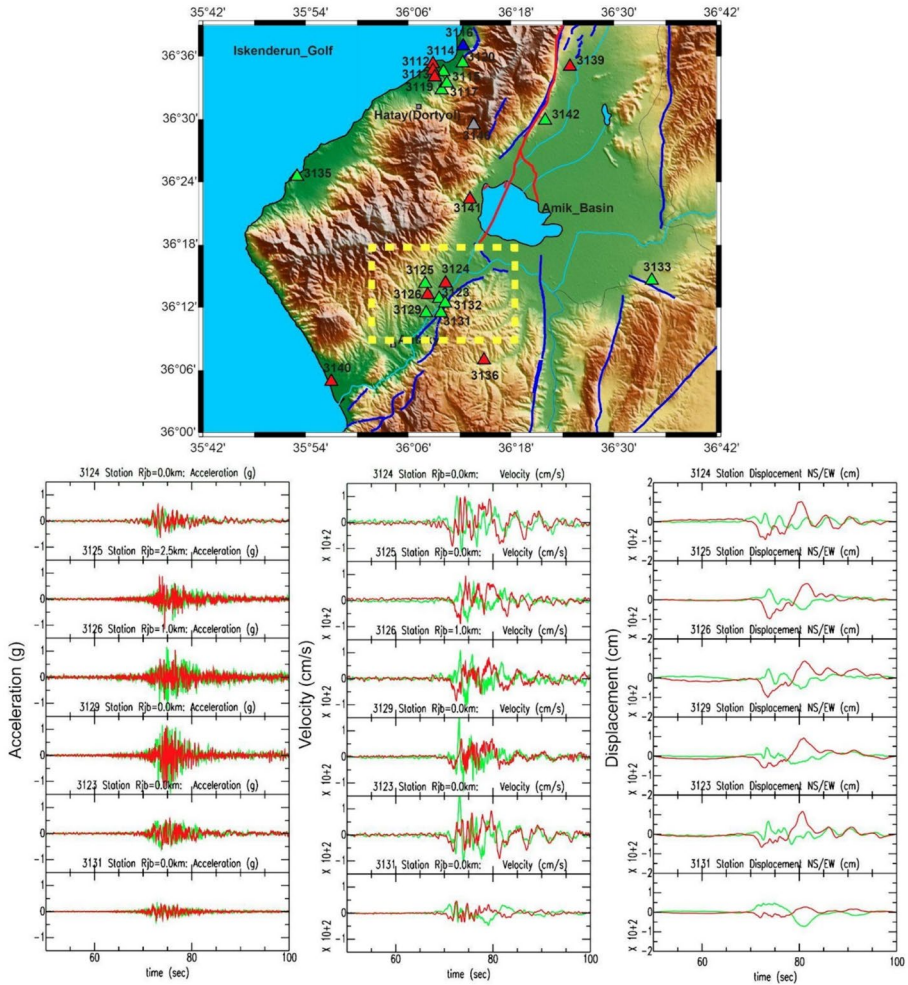


Fig. 5 Time series of the horizontal components (EW-red and NS-green) of recorded acceleration, along with processed velocity and displacements from the Pazarcık earthquake (Mw7.8), registered at stations within a small AFAD network close to the southern termination of the fault rupture: 3124, 3125, 3126, 3129, 3123, and 3131

predictions provided by the GMMs. Larger amplitudes indicate that structures of different heights may experience higher seismic loads than anticipated based on the GMM predictions.

For PSA ($T=0.2$ s), the amplitudes observed during the Elbistan earthquake closely align with the median curve of the two selected GMMs. However, in the case of the first mainshock (Pazarcık earthquake) several stations exhibit larger amplitudes compared to the model predictions. This difference becomes more pronounced at longer periods, namely PSA ($T=1.0$ s) and PSA ($T=2.0$ s). This effect is particularly prominent at the stations located on or near the fault rupture. When considering PSA ($T=1.0$ s) and PSA ($T=2.0$ s), the **KALE15** model shows larger spectral accelerations than the **BSSA14** model above 20 km, providing a slightly more accurate estimation for these two parameters.

However, the amplification effect of pulse-like ground motion resulted in a significant underestimation of response spectra at longer periods by empirical models, also partially observed in other GMPEs in distances up to 100 km (Graizer 2024). This observation suggests that the potential presence of a directivity effect results in higher velocities. Previous studies also discuss the possibility of the supershear earthquake rupture (Abdelmeguid et al. 2023; Delouis et al. 2023; Rosakis et al. 2023; Wan et al. 2024) during these earthquakes, which generated impulsive motion along the EAF.

The varying trends and differences observed in the two GMM models at longer and intermediate distances can be attributed to seismic wave propagation characteristics, such as the quality factor and the attenuation of seismic waves through Earth structures with altering crustal properties. Our direct comparison of ground motion data with global and region-specific GMMs suggests that the existing models did not fully capture the complex source and path effects observed during these earthquakes in the region.

The presence of these long-period, high-amplitude spectral accelerations has the potential to impact structures significantly. For a detailed examination of this topic and a comprehensive discussion, we invite readers to explore Sects. 6 and 7 of our analysis, where we thoroughly assess the implications of these findings on seismic hazard assessment and structural response.

5 Identifying the impulsive signals

In this section, the waveforms of the ground motion are examined, particularly those recorded near the fault rupture. Our primary objective is to identify any potential pulse-like signals within these waveforms. Impulsive motions can occur in fault-normal and parallel components in the strike-slip faults. In the normal motion components, horizontally polarized S waves (SH) can result in two-sided impulsive motions in the velocity domain. On the other hand, vertically polarized S waves (SV) can generate Gaussian-like velocity time histories, indicating permanent displacement in the strike parallel direction. These observations have been noted by researchers such as Somerville et al. (1997) and Burks and Baker (2016). Pulse-like impulsive signals in ground motions are easily distinguishable due to their unique spectral characteristics, marked by narrowband amplification in both elastic and inelastic spectra around the pulse period (T_p) (Kalkan and Kunnath 2006). These impulsive signals are well-known for placing greater inelastic demands on particular structures (Chioccarelli and Iervolino 2010; Iervolino et al. 2012). Hence, it is important to determine the impulsive signals and their periods.

The dense distribution of accelerometric stations along the EAFZ and the numerous ground motion traces recorded near-fault provide valuable insights into the directivity effect and enable the assessment of seismic rupture characteristics of the February 6th, 2023 earthquakes.

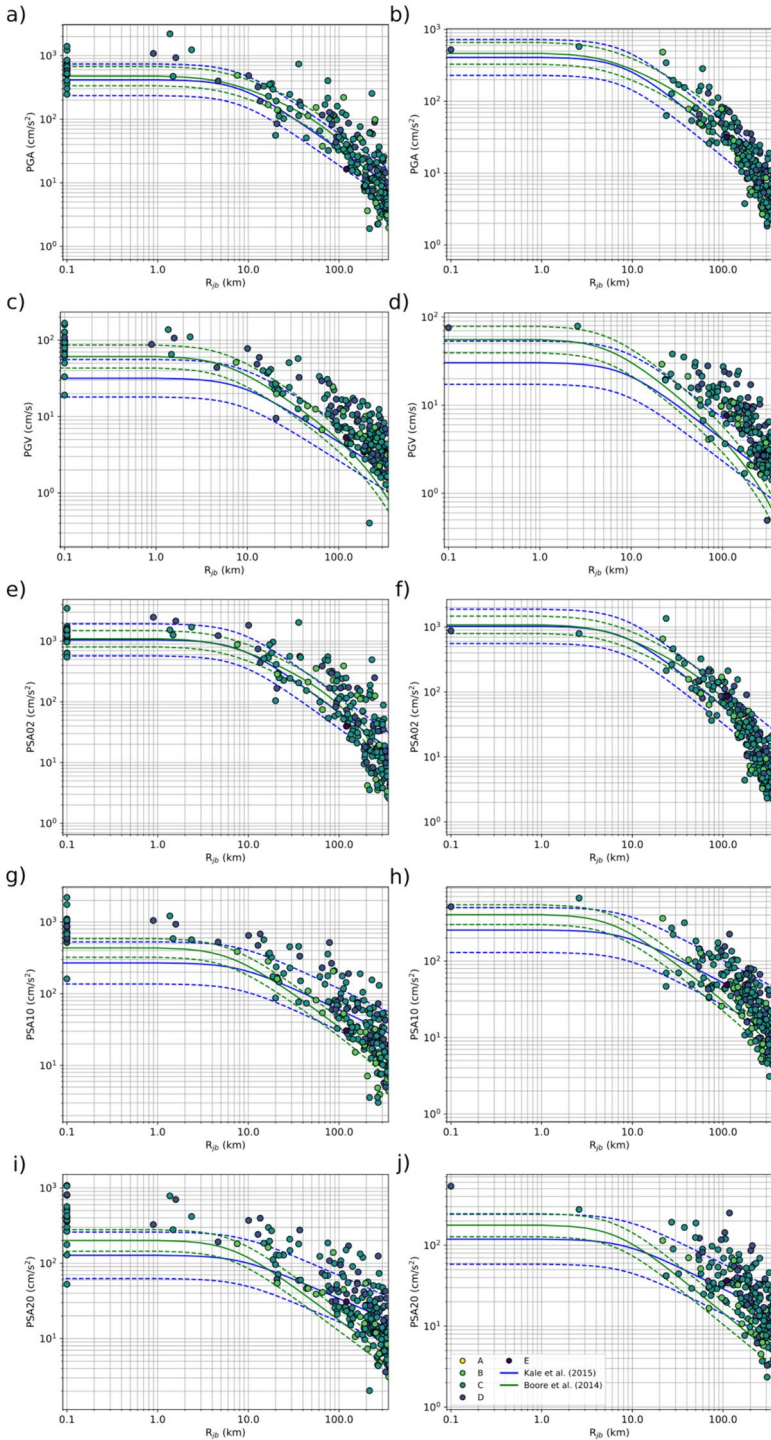
To detect the impulsive signals in the recorded ground motions, we applied a data pre-processing procedure similar to the one described in previous Sect. 3. Subsequently, we employed a method developed by Shahi and Baker (2014) to detect impulsive motion. This method utilizes wavelet transform analysis on two orthogonal components of ground motion, focusing in this study on the horizontal components. The method rotates the horizontal components to find the most energetic impulsive motion, which does not necessarily have to be in fault normal or fault parallel direction. A total of 36 impulsive motions were

Fig. 6 Observed **a** and **b** PGA, **c** and **d** PGV, **e** and **f** PSA ($T=0.2$ s), **g** and **h** PSA ($T=1.0$ s), and **i** and **j** PSA ($T=2.0$ s) as the maximum horizontal components for (left panel) the Pazarcık, and (right panel) the Elbistan earthquakes, compared to the BSSA14 and KALE15 models. Colored circles represent stations with different EC8 classes. Dashed lines present the \pm sigma of the GMPE models. GMPE models are produced by using fixed V_{s30} of 760 m/s

identified, with 28 corresponding to the Pazarcık earthquake and 8 to the Elbistan earthquake. The dense station coverage along the southern termination of the EAFZ allowed us to record 14 impulsive motions, which accounted for more than half of the impulsive motions observed in the Pazarcık earthquake, specifically in the Amanos segment. Along the fault plane, we observed large PGV values (78 cm/s to 156 cm/s) accompanied by pulse periods ranging from 2.6 to 12.0 s and several signals with interesting features (Fig. 7). Velocity traces of stations 0120, 0213, 3123, 3137, 3146, 3147, 4616, 8002, and NAR record impulsive motions during the Pazarcık earthquake, and stations 0118, 0134, and 4612 record impulsive motion during the Elbistan earthquake. The NAR station, located close to the Pazarcık fault, exhibits a clear example of the directivity effect with its large magnitude and long-period behavior at the beginning of the seismic trace.

In a previous study by Rosakis et al. (2023), a super-shear in the Pazarcık fault was suggested. Station 0213, situated near the Pütürge segment at the northeastern end of the mainshock rupture, captured only the initial part of the earthquake but exhibited clear impulsive motion. Stations along the Amanos segment at the southwestern termination of the rupture, extending up to Hatay, recorded numerous impulsive motions. Stations 3123, 3137, 3146 and 3147 displayed low-amplitude earthquake motion before the arrival of impulsive motion, likely indicating that this segment ruptured after the Pazarcık segment. The earthquake energy causing impulsive motions in stations like NAR and 0213 might have been attenuated at the southern stations. The maximum amplitude before the impulsive motion in the stations along the Amanos segment in the south aligns with the GMMs, considering the epicentral distance is around 100 km. The energy released by the Amanos segment, heading towards Hatay, may have generated impulsive motions in these stations. Stations 3137 and 3146 exhibit long periods and relatively large amplitude signals. In stations 3123, 3124, 3126, and 3129 in Hatay, T_p is low, whereas PGVs are very large (≥ 100 cm/s). This observation can be attributed to the soil conditions of the site. For example, station 3137 is located on a cliff, and the main geological feature is basalt (AFAD 2023a). In contrast, station 3123 is situated in alluvial soil with sand as the predominant geological feature (AFAD 2023b). Local soil conditions may have also contributed to the presence of impulsive signals in some cases, as suggested by Cork et al. (2016) in Hatay. It should be noted, however, that the observed PGVs are very large in several stations with presence of pulse, indicating a strong influence of the near fault effects rather than local soil conditions in these high PGV cases.

In the case of the Elbistan earthquake, only one station was located on top of the rupture area (station 4612). However, impulsive motions were recorded at R_{jb} distances up to



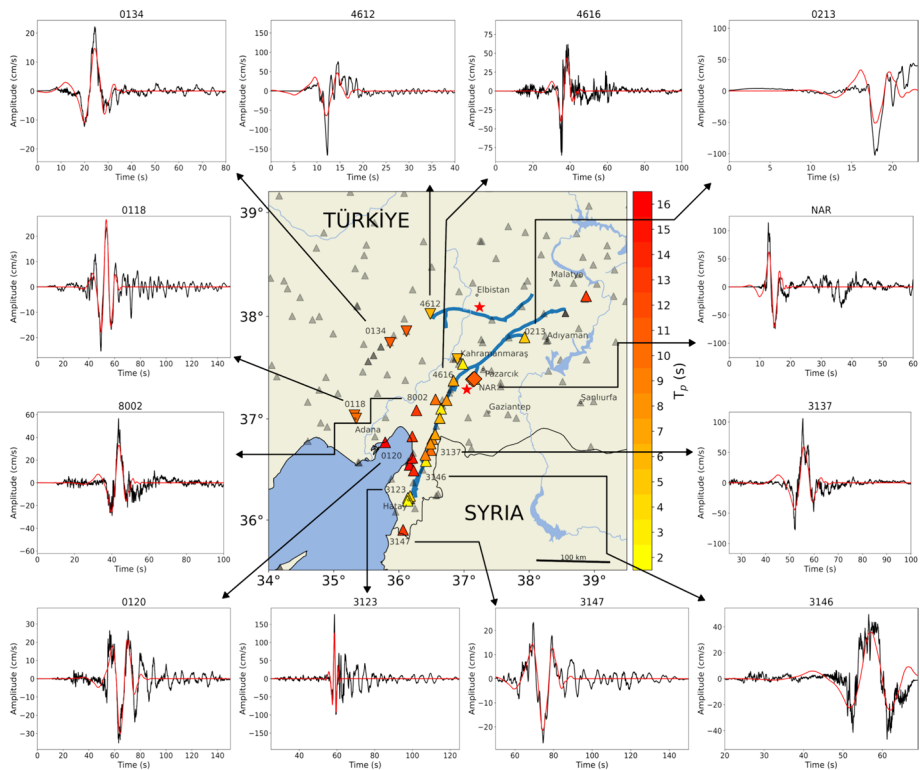


Fig. 7 Distribution of impulsive signals for the Pazarcık (Mw7.8) and the Elbistan (Mw7.5) earthquakes. Stations are plotted as triangles, reverse triangles, and diamonds represent stations with impulsive motions in the Pazarcık, the Elbistan, and both earthquakes, respectively. A list of stations that show impulsive motion is given in Table S3 and Table S4. Red waveforms represent the wavelet fit by the method of Shahi and Baker (2014). Blue lines present the fault rupture of the February 6th, 2023 Kahramanmaraş, Türkiye, Earthquake Sequence as delivered by USGS

150 km. The widespread occurrence of impulsive motions can be partially attributed to the directivity effect. Notably, these impulsive motions were not only observed in far-field regions but also exhibited long periods (e.g., station 0118). The impulsive motion recorded at station 4612 can be linked to the directivity effect as the concentration of the seismic energy over a relatively short amount of time and due to its proximity to the ruptured fault with a large PGV (164 cm/s) value.

The occurrence of impulsive motion is also observed in other studies that use different pulse detection algorithms (Ertuncay and Costa 2024) and these impulsive motions create large inelastic displacement ratios (Ucar and Merter 2024).

6 Comparison of the acceleration response spectra with the code and with the energy based spectra

In this section, we present the processed acceleration response spectra of a large set of recordings, comparing them to the acceleration design spectrum of the most recent Turkish seismic code of 2019. Acceleration spectral values have traditionally played a major role in seismic analysis and the design of engineering structures.

However, in recent years, the energy concept has gained favor among researchers due to its capacity to encompass the full duration and frequency spectrum of motion, offering a more comprehensive understanding of how ground motion impacts structures. Currently, seismic codes do not specify an energy spectrum. Nevertheless, there is an expectation that upcoming seismic codes will integrate energy-related terms into their definitions of seismic hazard and structural resistance capacity. To better explain the energy spectrum, the structural response spectra at two selected stations, 4613 and 4630, are presented in Fig. 8. The first row shows the structural response resultant spectra of the lateral ground motions using the square root of the sum squares (SRSS) rule, and the second row displays the energy imparted to the structure. While the impact of the recorded ground motion on the structural response is evident, the energy term, representing the cumulative summation of ground excitation on the structure, inherently takes the duration and frequency content of the acceleration records into account. In Fig. 8, acceleration spectral values of both stations are almost identical to an elastic single-degree-of-freedom (SDOF) system. However, energies imparted to the structure significantly differ for both stations. Such a discrepancy may lead to underestimation of the severity of ground motion on the structures and raises question of whether the energy spectra should be a parameter used to relate structural response to the earthquakes, providing a better understanding of seismic intensity and structural response (Dindar et al. 2015).

The energy imparted into any structure is resisted by the mechanisms that either dissipate or survive throughout the excitation period. One of the mechanisms dissipating the imparted energy is the occurrence of damage to the structural members. Several studies

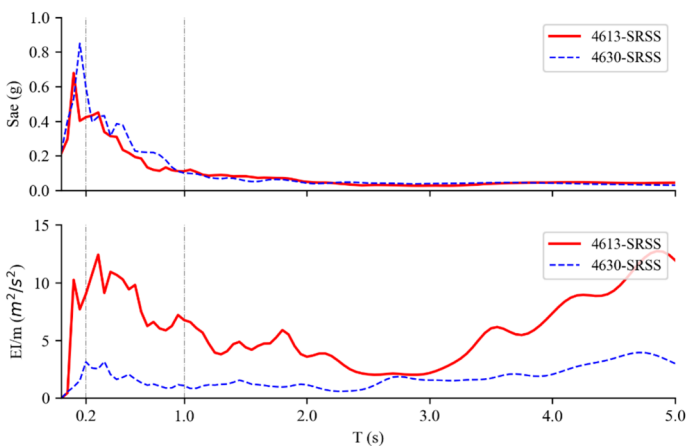


Fig. 8 The mass-normalized energy spectrum is depicted, with a focus on AFAD stations 4613 and 4630. This analysis underlines the similarity in acceleration spectra shapes at $T=0.2$ and 1.0 s, yet reveals substantial differences in the energy spectra. These differences underscore the considerable seismic demand on the structures' period

have demonstrated a direct relationship between the energy dissipation of the members and damage because the plastic deformation of the member requires irrecoverable energy diminishing (Cheng et al. 2021; Grammatikou et al. 2022). Based on the evident correlation of damage with the energy spectrum as reported in the literature, it is clear that the energy concept has the potential to help unveil the complex nature of the relationship between strong ground motion and observed structural damage. The discrepancy between response spectra and the energy spectra, revealed for stations 4613 and 4630 in this study, brings into question whether the energy spectra should be one of the parameters used in relating the structural response to the earthquakes since it provides better understanding of the seismic intensity and the structural response.

Although briefly presented here (Fig. 8) for two stations, the energy spectrum, intended for potential further uses, is not within the main scope of this study and this is not further examined. It is noteworthy, however, that a better understanding of ground motions could be utilized as more studies on the correlation of damage to the energy spectrum become available.

The relationship between the observed response spectra and those from the current seismic hazard map has also been examined in this study. Since the 1940s, there have been thirteen Turkish seismic codes and seven seismic hazard maps released by Turkish government authorities. The current building stock in Turkey can be classified into three major groups concerning the seismic design code releases: pre-2000, 2000–2018, and finally, post-2018. Pre-2000 hazard maps were based on seismic zones, leading to the inclusion of region-specific coefficients in the acceleration response spectrum formulation. These coefficients are highly questionable for areas on the zone contours (Akkar et al. 2018). In contrast, the 2018 hazard map relies on grids where seismic hazard intensities are defined. Other features introduced in the TBDY 2018 include revised spectral values in the long-period region, as well as vertical ground motion components and displacement spectra. Contrary to previous versions, the TBDY 2018 defines probabilistic ground motion intensities at four distinct levels, DD1 to DD4. Both the 1998 and TBEC (2007) codes defined only the DD2 level (475-year), with DD1 (2475-year) implicitly recommended as 1.5 times greater than DD2 in the 2007 code. Therefore, the 1998–2007 period (both relying on the same hazard map and spectrum definition) and TBDY 2018 are noteworthy when comparing seismic demand in terms of spectral acceleration across soil class, intensity, and vibration period.

Figure 9 shows two response spectra (acceleration) for both horizontal and vertical components, comparing them with the design spectra corresponding to return periods of 475 years (DD2) and 2475 years (DD1) derived from previous and recent building codes. Station 3126, located on site class D over the fault rupture, exhibits similar acceleration characteristics in both vertical and horizontal directions. The response spectra for both EW and NS components show amplification around 0.2 s, peaking at 5095 cm/s^2 for the NS component. These values surpass the design spectrum for both DD1 and DD2. Station 3138, situated in Hatay on site class B over the fault rupture, displays broadband period content in the horizontal response spectra, surpassing the design spectrum for DD2. Despite being on stiff soil conditions, both horizontal components show clear amplifications at longer periods, with one being stronger around 0.7–1.2 s. Both horizontal and vertical components' response spectra exceed the design spectrum for DD1 at periods longer than 0.2–0.5 s. The observed high velocity amplitudes with short duration suggest potential forward directivity effects, represented by impulsive pulses, especially in this area where building damage was pronounced.

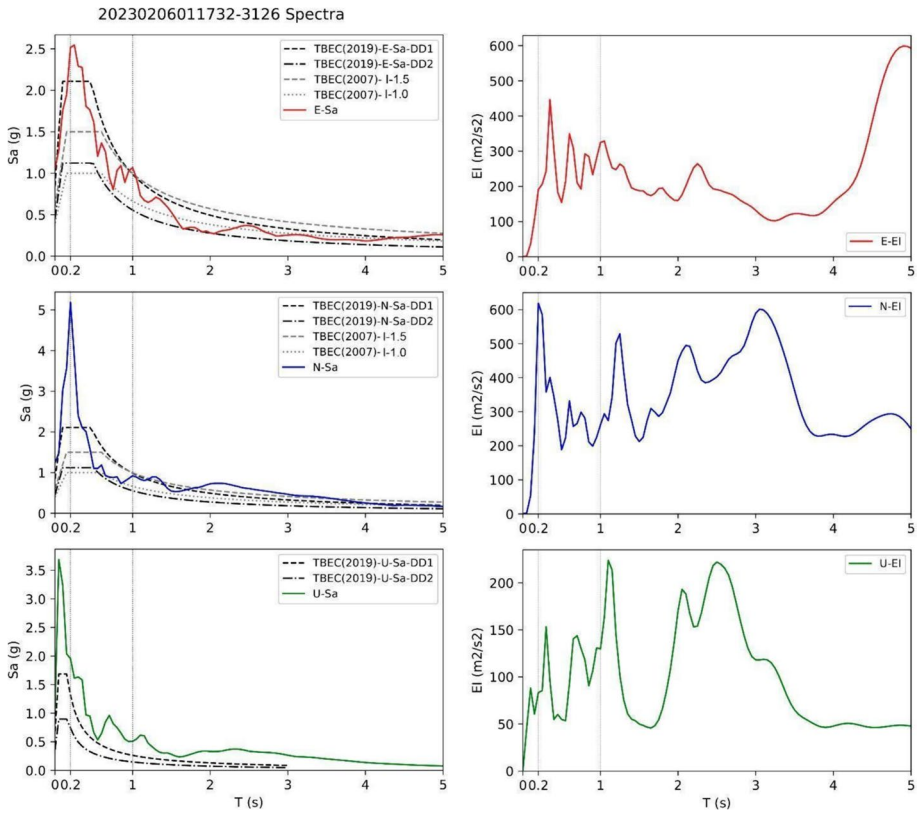


Fig. 9 Comprehensive view of the seismic data, showcasing the recorded three-component ground accelerations. The figure includes acceleration response spectra (with 5% damping) with the previous and most recent building code (TBDY, 2018) for comparison, and the energy spectra. Specifically, the selected stations, namely 3126 (upper panel), and 3138 (lower panel) from the Pazarcik (Mw7.8) mainshock, are examined

Having studied the generated spectra, we find that a significant number of stations exceeded the design-level earthquake intensities DD2 and DD1 not only horizontally but also in the vertical direction. In Fig. 10, we present the ratio of both horizontal and vertical spectral values of 31 stations located near the fault rupture to TBDY 2018’s (a) DD2 and (b) DD1 level values. The horizontal components of each station were converted to resultant values by taking the geometric mean to be consistent with TBDY 2018. The following results were obtained from this comparison:

- Five AFAD stations (3125, 3126, 3129, 3135, and 3141) have horizontal spectral acceleration values greater than the TBDY 2018 DD2 level at all period ranges. Only two stations (4408 and 4630) were completely below the DD2 level, and the remaining 24 stations were partially above the DD2 level.
- The majority (a total of 23 stations) of the vertical spectra are above the DD2 level, except for station 4630.
- Eight of the stations located in Hatay province are above the DD2 level.
- None of the horizontal spectra are above the DD1 level.

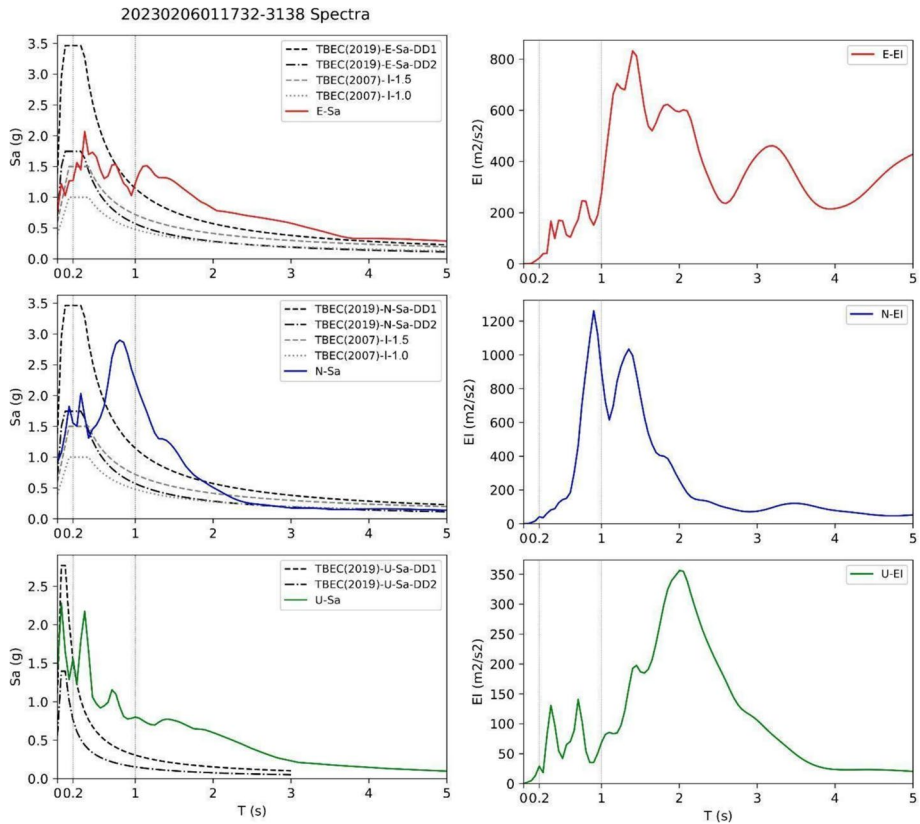


Fig. 9 (continued)

- The lateral response spectra of thirteen stations are above the DD1 level at different periods.
- Interestingly, station 3126 presents vertical spectra values larger than the DD1 level at all periods.

7 Evaluation of the observed structural damages

The February 6th earthquake sequence, characterized by large-magnitude main shocks and complex fault structures covering a wide geographical area, resulted in overwhelming destruction to the built environment. Major urban centers were severely damaged or reduced to ruins. Reconnaissance teams, including Cetin et al. (2023) and Ozkula et al. (2023), collected data illustrating the performance of structures. This not only highlighted apparent structural deficiencies and recurrent construction mistakes but also provided a grim estimate of the financial support needed for reconstruction. As reinforced buildings constitute the majority of the building stock, their prompt assessment after the earthquake was crucial for restoring normalcy in the affected areas. As the extent and nature of the structural damage became clear over time, a striking

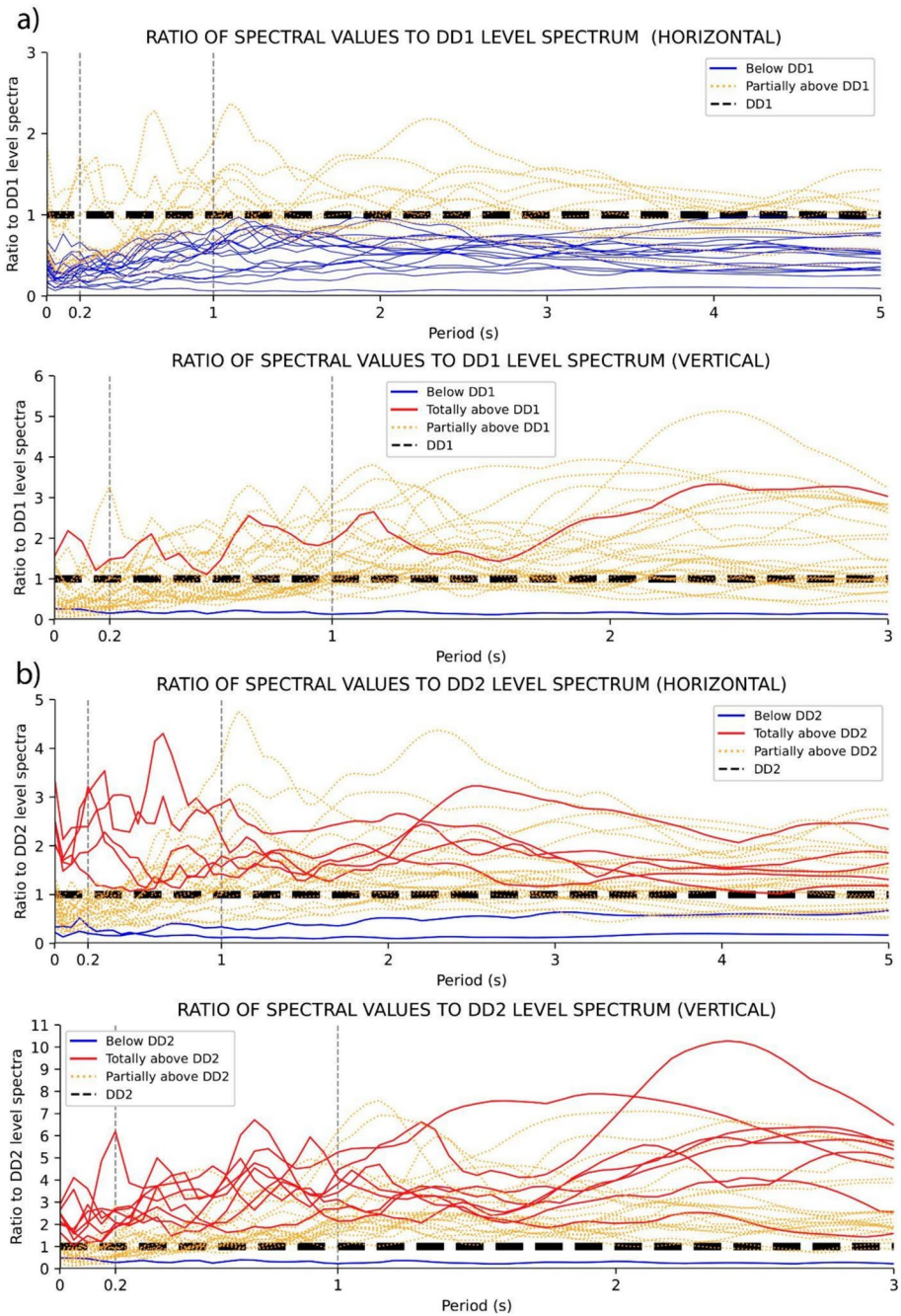


Fig. 10 The ratio of spectral values at AFAD stations to TBDY 2018 for both DD2 (a) horizontal-vertical components and DD1 (b) horizontal-vertical components. Stations 3125, 3126, 3129, 3135, and 3141 exhibit spectral values greater than TBDY 2018 DD2 values across all periods



Fig. 11 Post-2000 buildings in İskenderun and in Hatay-Antakya, MCG Tower (above) and Ronisans Residence (below), built in 2009–2011, suffered uprooting collapse, claiming more than 900 lives combined

image emerged from the earthquake zone – the uprooting of large reinforced concrete (RC) buildings.

Illustrated in Fig. 11 through a couple of examples, the uprooting of these buildings resulted in the loss of hundreds of lives in a single structure. The figure shows collapsed buildings in Hatay (Antakya and İskenderun), constructed post-2000 according to the TBEC (2007) and designed for the DD2 level of hazard. These buildings, constructed in accordance with modern seismic hazard and design regulations, were not anticipated to collapse. In addition to well-known issues in Turkish construction practices, such as a lack of strict control during construction, deviation from code-specified details, and departure from basic seismic design principles, the level and nature of seismic demand likely played a significant role in the collapse of these and many similar buildings. One of the main characteristics of the buildings, as depicted in Fig. 11, is their relatively tall stature (10 stories and above), resulting in long periods of around 1 s. Additionally, their collapse differs from the classic pancake-type collapse observed in previous Turkish earthquakes. These structures exhibit an ‘uprooting collapse’ mechanism, indicating a significant exceedance of their capacity. This phenomenon has never been observed before, at least not to this extent.

The collapse of the uprooted tall reinforced concrete structures raises questions about whether the seismic hazard in the long-period part of the design spectra aligns with the observed response spectra. In addition to the inherent deficiencies in Turkish construction practices, the preference for certain structural systems that did not ensure satisfactory seismic performance proved critical. This was particularly evident given the strong seismic demand, which exceeded the design values several times in many locations. The map in Fig. 12 clearly illustrates that the design basis spectral accelerations are surpassed not only for the 475 return period, for which ordinary residential buildings are designed, but also for the 2475 return period.

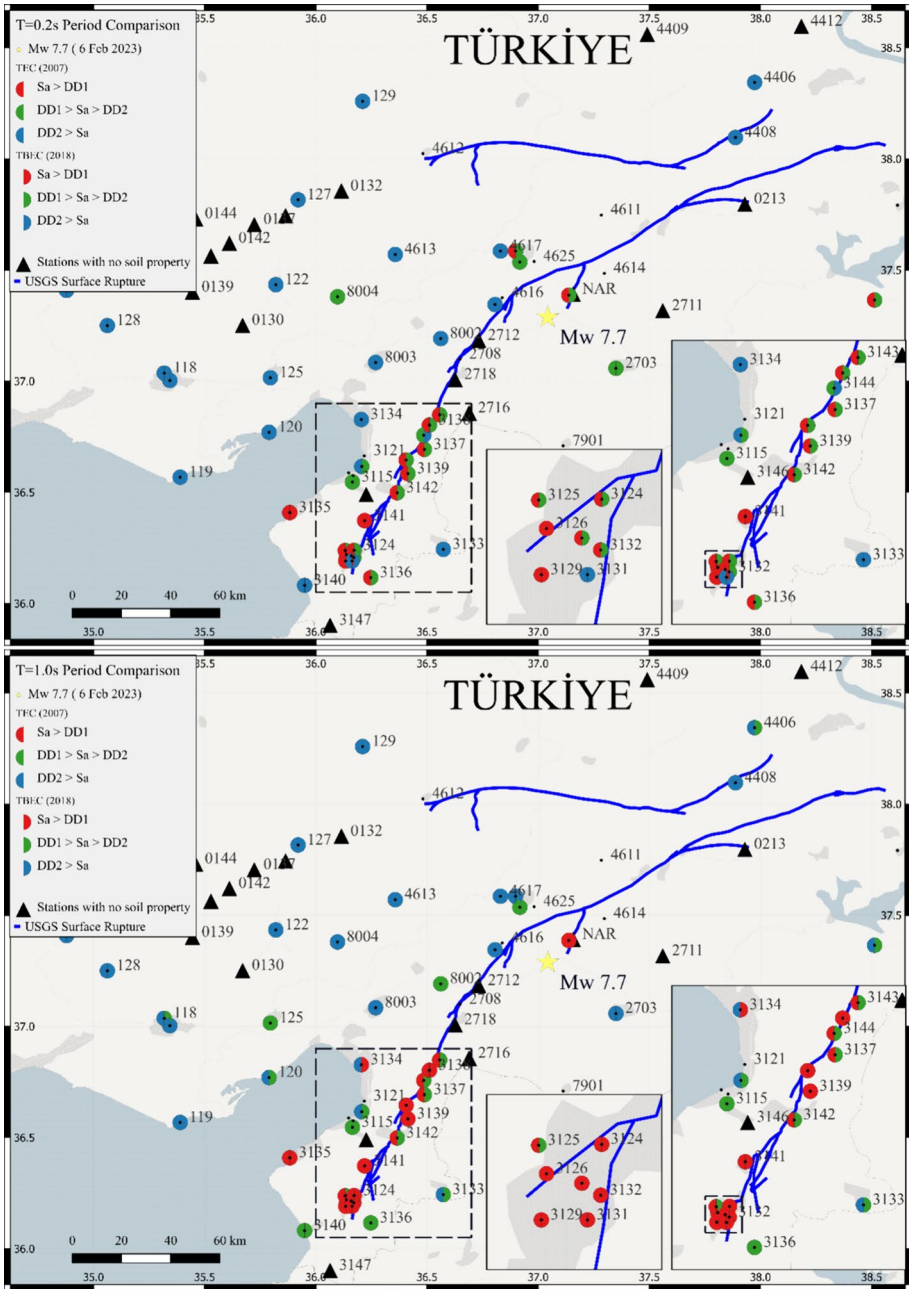


Fig. 12 Comparison of the **a** short (0.2 s) and **b** long (1.0 s) period spectral accelerations of recorded motion to the 2007 and 2019 Turkish seismic design codes

In Fig. 12a, a comparison of spectral accelerations at short periods ($T=0.2$ s) is presented. This short period range corresponds to buildings with 1–2 stories, short and stiff buildings, and rural masonry-type buildings. The comparison is made between the 5% damped acceleration response spectra of the recorded motions and those of the TBEC (2007) and TBDY 2018 codes, using AFAD station locations. While station data are usually well-documented, some stations lack data on soil properties, indicated by black triangles. Soil data is necessary to construct the corresponding acceleration response spectrum. In the comparison, the geometric mean of the recorded two horizontal spectra is compared to the code spectra at DD2 and DD1 levels, corresponding to seismic hazard levels of 475 and 2475 years return period, respectively. The 2018 Turkish seismic hazard map readily provides hazard parameters for these two levels, while the importance factor of 1.5 is used for the spectra of the 2007 Code to transform the DD2 spectrum to DD1 for comparison purposes. In Fig. 12a, the red circles or semi-circles indicate excess values compared to the DD1 level of the code spectra. The DD1 level is beyond the seismic design levels used for ordinary residential buildings (DD2), suggesting that the recorded motion significantly exceeds the design basis. In the short period, DD1 spectra of the TBEC (2007) are exceeded along the fault rupture line, especially in the south (Hatay province).

Similarly, Fig. 12b provides a comparison between the recorded motions and the TBEC (2007) and TBDY 2018 code spectra, focusing on long periods ($T=1.0$ s). This long period range is usually outside of the plateau (constant acceleration range) of the design response spectra, in the declining branch. It corresponds to mid-to-high-rise RC buildings (approximately 8–12 stories) and rather flexible structures. The use of short and long periods as 0.2 s and 1.0 s comes from a procedure established in the National Earthquake Hazard Reduction Program, NEHRP, in the United States, U.S. (Building Seismic Safety Council, BSSC 2001), where hazard data at these two periods were turned into a smooth design spectrum, highlighting the importance and wide usage of these two periods. In terms of structural damage, Fig. 12a indicates that the DD1 level was exceeded for both code spectra, especially in the south part of the ruptured fault. This observation aligns with the catastrophic collapse of new (post-2000) tall structures in uprooting fashion in the south of the fault rupture, specifically in Hatay province. The excess of the design basis is concentrated along the fault rupture, aligning with the reported damages (Vuran et al. 2023). Particularly for structures with a high fundamental period (1.0 s and above), the exceedance of observed spectral accelerations is more pronounced. The map in Fig. 12b reveals a regional clustering of very high spectral accelerations at longer periods. A closer examination, as depicted in Fig. 9 and 10, shows that in Hatay province (AFAD station codes starting with 31), located at the southern end of the mainshock rupture and experiencing directivity effects, almost all stations exhibited significantly higher spectral acceleration demand at longer periods, surpassing the 2475-year return period design basis. This observation, coupled with the exceptionally high concentration of structural damage in Hatay, especially in Antakya, corresponds to the large amplitude velocity pulses shown in Sect. 5, Fig. 7. The consistent excess of spectral demand at long periods also correlates with the well-known fact that peak ground velocity is associated with structural damage. This explains the widespread damage in Antakya, where the staggering 181.82 cm/s velocity pulse from station 3123 was recorded, as shown in Fig. 7. In addition to the damage to ordinary buildings, several striking uprooting collapses were reported in Antakya.

Pulse-like ground motions have been observed in many significant earthquakes worldwide. For instance, the strike-slip Mw7.0 Kumamoto earthquake in Japan was

significantly affected by directivity effects, with the near-fault ground motion response spectra in the sensitive periods of 0.5–2.0 s for building structures even exceeding those of the Mw7.9 Wenchuan earthquake (Xie et al. 2017). These long-period ground motions and large velocity pulses, particularly those formed in the rupture forward direction, often cause major and irreparable damage to structures and needs to be taken into account for future ground motion models and seismic hazard assessment (Champion and Liel 2012).

8 Conclusion

In this study, we analyzed the ground motion characteristics of the main shock in terms of peak ground acceleration (PGA), peak ground velocity (PGV), and pseudo-acceleration response spectra (with a 5% damping ratio). Specifically, we compared the pseudo-acceleration response spectra for horizontal directions with the design spectrum and the new Turkish building code. Additionally, we examined source-related effects, including pulse-like ground motion induced by the February 6th earthquakes. Finally, the observed structural damages are analyzed and correlated with the recorded ground motions in the heavily damaged areas.

Key findings can be summarized as follows:

- (1) On February 6th, the earthquake doublet generated remarkably high accelerations, as evidenced by numerous strong motion recordings along the fault rupture. Many stations recorded the highest ground motions, with values exceeding 1000 cm/s^2 and 100 cm/s even at longer periods,—marking some of the highest peak ground accelerations and velocities ever documented. Most PGAs and PGVs, along with the permanent ground displacement, were particularly elevated in Hatay Province within the Amik basins, located approximately 200 km southwest of the epicenter. These elevated ground motions are likely due to a combination of site-related basin and source-related directivity effects, which requires further investigation.
- (2) A comparative analysis of recorded ground motion amplitudes was conducted, using two ground motion models, **KALE15** and **BSSA14**, to assess their performance in representing the ground motion characteristics of the region. Visual inspection indicated general agreement between recorded PGA values and the median estimations of both models across all R_{jb} distances. However, the median predictions for PGV exhibited significant differences between the selected GMMs, resulting in noticeable variations compared to recorded PGVs distributions. Both GMM models consistently underestimated observed PGVs. Underestimation of the amplitudes in longer periods ($PSA \geq 1.0 \text{ s}$), along with PGV, exceeds even plus one sigma. In the Pazarçık earthquake, stations close to the rupture have a large range of amplitudes in all compared metrics, indicating complex rupture features along the segments. Stations with large ground motion values can be linked to the earthquake rupture characteristic and directivity effect. Moreover, to more accurately assess the GMM performance relative to the data, further investigation is necessary, including the computation of total residuals and consideration of appropriate path and site conditions.
- (3) Large amplitudes in velocity waveforms were identified as impulsive motions in both earthquakes mostly in near-fault regions. In the Pazarçık earthquake, 28 impulsive motions with T_p up to 15.6 s were detected, whereas in the Elbistan earthquake, 8 impulsive motions with T_p up to 11.4 s were observed. The high concentration of

impulsive motions in the near-fault areas may be caused by the earthquake rupture kinematic and results such as the strong directivity effect. Nevertheless, impulsive motions in far-field regions may have more complex reasons, such as local site effects and the detailed characteristics of source rupture that need further investigation. A high concentration of structural damage was observed specifically in Hatay province, located at the southern end of the mainshock rupture, corresponding to the region where these large amplitude velocity pulses were detected.

- (4) The horizontal and vertical seismic demands, assessed through pseudo-acceleration spectral responses, were particularly severe in both the short and long natural vibration period ranges of structures, proximity of 0.2 and 1 s, respectively. The computed spectral accelerations surpassed the values of not only the 475 year return period in which ordinary residential buildings are designed, but also the 2475 return period which is accounted the maximum credible earthquake level in the design of critical structures such as hospitals, high-rise buildings bridges etc. This underscores the considerable potential for damage to medium-rise buildings (over 5 stories). Additionally, the vertical spectral demands, not generally considered in the seismic design, were also found to be remarkably high in these earthquakes.
- (5) Locations with extremely high PGV values coincided with collapses of tall reinforced concrete structures, where the uprooting type of collapsed mechanism differed from the pancake-type collapse seen in building, despite the fact that those were constructed according to modern seismic design codes. This highlights the impact of the large impulsive nature of the records, inadequately addressed in current seismic design codes. Therefore, this paper includes an introductory discussion of the energy-based spectrum which gives better understanding of the severity of the ground motions on the structural damage. The conventional response spectrum construction method relied on the maximum absolute response of a Single Degree of Freedom, SDOF system, disregarding the duration and frequency content of the excitation motion, thus neglecting cumulative effects of the excitation. In contrast, the energy spectrum explicitly integrates ground motion characteristics with structural response.

In conclusion, the finding of this study emphasizes the need to revise earthquake-resistant design standards for certain type engineering structures, particularly those with long-periods due to their flexible load-bearing systems, considering the amplification effect of pulse-like ground motions.

Supplementary Information The online version contains supplementary material available at <https://doi.org/10.1007/s11069-024-06856-y>.

Acknowledgements We extend our sincere gratitude to all the individuals working at the Earthquake Department of the Disaster and Emergency Management Presidency, AFAD, Kandilli Observatory and Earthquake Research Institute, KOERI, for their dedicated efforts in deploying seismic stations and generously providing the data that served as the foundation for our scientific research and study. The study was partially funded by the Center for the Seismic Hazard Studies, CPS, at Istituto Nazionale di Geofisica e Vulcanologia (INGV) of Rome, Italy. Dr. Ertuncay received financial support from the Italian Civil Protection Department—Presidency of the Council of Ministers (DPC) under the agreement between DPC and University of Trieste for the accelerometric monitoring of the Friuli Venezia Giulia Region (agreement number: RAN-2020-2022 CUP: J91F20000110001) and RETURN—multi-Risk sciEnce forresilienT commUnities undeR a changiNg climate (CUP: F83C22001660002), funded by the European Union—Next Generation Unit. We thank Jonathan Ford from the Department of Geophysics, National Institute of Oceanography and Applied Geophysics (OGS), for proofreading the paper.

Author contribution Conceptualization, A.A., A.A.D., D.E.; Methodology, A.A., A.A.D., D.E.; Software, A.A., A.A.D., D.E.; Validation, A.A., A.A.D., D.E.; Formal analysis, A.A., A.A.D., D.E.; Investigation, A.A., I.E.B., E.S., D.E.; Resources, A.A., A.A.D., D.E.; Data Curation, A.A., A.A.D., D.E.; Writing—Original Draft, A.A., A.A.D., I.E.B., E.S., D.E. D.C.; Writing—Review & Editing, A.A., A.A.D., I.E.B., E.S., D.E., D.C.; Visualization, A.A., A.A.D., D.E., D.C.; Supervision, A.A.

Funding Open access funding provided by Istituto Nazionale di Geofisica e Vulcanologia within the CRUI-CARE Agreement. This research did not receive any specific grant from funding agencies in the public, commercial, and not-for-profit sectors.

Data availability Data processing in Sect. 4 was performed using the ObsPy Python package (Beyreuther et al. 2010) and Seismic Analysis Code (SAC) v.101.6 (Goldstein and Snoko 2005; Goldstein et al. 2003). Figures were created using Generic Mapping Tools v.4.5.3 (The GMT Home Page (hawaii.edu), last accessed in September 2023, Wessel et al. 2013) and the Cartopy Python package (Met Office 2010–2015). Strong ground motion data were obtained from the Disaster and Emergency Management Presidency (AFAD) website (<https://tadas.afad.gov.tr/>; and last accessed September 2023) and from the Kandilli Observatory and Earthquake Research Institute website (WebDC3 at eida.koeri.boun.edu.tr; last accessed September 2023). More information on the Pazarcik and Elbistan earthquakes were obtained from the U. S. Geological Survey website, (M 7.8—Pazarcik earthquake, Kahramanmaraş earthquake sequence ([usgs.gov](https://www.usgs.gov)), and M 7.5—Elbistan earthquake, Kahramanmaraş earthquake sequence ([usgs.gov](https://www.usgs.gov)), last accessed September, 2023).

Declarations

Conflict of interest The authors declare that they have no known competing financial interests or personal relationships that could have appeared to influence the work reported in this paper.

Open Access This article is licensed under a Creative Commons Attribution 4.0 International License, which permits use, sharing, adaptation, distribution and reproduction in any medium or format, as long as you give appropriate credit to the original author(s) and the source, provide a link to the Creative Commons licence, and indicate if changes were made. The images or other third party material in this article are included in the article's Creative Commons licence, unless indicated otherwise in a credit line to the material. If material is not included in the article's Creative Commons licence and your intended use is not permitted by statutory regulation or exceeds the permitted use, you will need to obtain permission directly from the copyright holder. To view a copy of this licence, visit <http://creativecommons.org/licenses/by/4.0/>.

References

- Abbaszadeh Shahri A, Shan C, Larsson S, Johansson F (2024) Normalizing large scale sensor-based MWD data: an automated method toward a unified database. *Sensors* 24:1209. <https://doi.org/10.3390/s24041209>
- Abdelmeguid M, Zhao C, Yalcinkaya E, Gazetas G, Elbanna A, Rosakis A (2023) Dynamics of episodic supershear in the 2023 M 7.8 Kahramanmaraş/Pazarcik earthquake, revealed by nearfield records and computational modeling. *Commun Earth Environ* 4(1):456. <https://doi.org/10.1038/s43247-023-01131-7>
- AFAD (2023a) 06 Şubat 2023 Pazarcik-Elbistan Kahramanmaraş (Mw: 7.7 – Mw: 7.6) Deprem Raporu (in Turkish). Available from (Last access: July 2023).
- AFAD (2023b) <https://tadas.afad.gov.tr/station-detail/2306>, last access: 25/10/2023
- AFAD (2023c) <https://tadas.afad.gov.tr/station-detail/2292>, last access: 25/10/2023
- Akkar S, Azak T, Çan T, Çeken U, Demircioğlu Tümsa MB, Duman TY, Erdik M, Ergintav S, Kadiriöğlu FT, Kalafat D, Kale Kartal RF, Kekovalı K, Kılıç T, Özalp S, Altuncu Poyraz S, Şeşetyan K, Tekin S, Yakut A, Zülfiyar Ö (2018) Evolution of seismic hazard maps in Turkey. *Bull Earthq Eng* 16(8):3197–3228. <https://doi.org/10.1007/s10518-018-0349-1>
- Akkar S, Kale Ö, Ansari A, Durgaryan R, Gündoğan A, Hamzehloo H, Harmandar E et al (2014) EMME strong-motion database serving for predictive model selection to EMME ground-motion logic-tree applications. In: Proceedings of the second European conference on earthquake engineering and seismology.

- Aktug BA, Ozener H, Dogru A, Sabuncu A, Turgut B, Halicioglu K, Yilmaz O, Havazli E (2016) Slip rates and seismic potential on the East Anatolian fault system using an improved GPS velocity field. *J Geodynam* 94:1–2. <https://doi.org/10.1016/j.jog.2016.01.001>
- Allen M, Jackson J, Walker R (2004) Late Cenozoic reorganization of the Arabia-Eurasia collision and the comparison of short-term and long-term deformation rates. *Tectonics*. <https://doi.org/10.1029/2003TC001530>
- Ambraseys NN (1989) Temporary seismic quiescence: SE Turkey. *Geophys J Int* 96(2):311–331. <https://doi.org/10.1111/j.1365-246X.1989.tb04453.x>
- Ambraseys NN (2009) Earthquakes in the Mediterranean and Middle East: a multidisciplinary study of seismicity up to 1900. Cambridge University Press
- Ambraseys NN, Jackson JA (1998) Faulting associated with historical and recent earthquakes in the Eastern Mediterranean region. *Geophys J Int* 133(2):390–406. <https://doi.org/10.1046/j.1365-246X.1998.00508.x>
- Ancheta TD, Darragh RB, Stewart JP, Seyhan E, Silva WJ, Chiou B-J, Wooddell KE et al (2014) NGA-West2 database. *Earthq Spectra* 30(3):989–1005. <https://doi.org/10.1193/070913EQS197M>
- Barbot S, Luo H, Want T, Hamiel Y, Piatibratova O, Javed MT, Braitenberg C, Gurbuz G (2023) Slip distribution of the February 6, 2023 Mw 7.8 and Mw 7.6, Kahramanmaraş, Turkey earthquake sequence in the East Anatolian Fault Zone. *Seismica*. <https://doi.org/10.26443/seismica.v2i3.502>
- Beyreuther M, Barsch R, Krischer L, Megies T, Behr Y, Wassermann J (2010) ObsPy: a Python toolbox for seismology. *Seismol Res Lett* 81(3):530–533. <https://doi.org/10.1785/gssrl.81.3.530>
- Bletery Q, Cavalié O, Nocquet JM, Ragon T (2020) Distribution of interseismic coupling along the North and East Anatolian Faults inferred from InSAR and GPS data. *Geophys Res Lett*. <https://doi.org/10.1029/2020GL087775>
- Boore DM, Bommer JJ (2005) Processing of strong-motion accelerograms: needs, options and consequences. *Soil Dyn Earthq Eng* 25(2):93–115
- Boore DM, Azari SA, Akkar S (2012) Using pad-stripped acausally filtered strong-motion data. *Bull Seismol Soc Am* 102(2):751–760. <https://doi.org/10.1785/0120110222>
- Boore DM, Stewart JP, Seyhan E, Atkinson GM (2014) NGA-West2 equations for predicting PGA, PGV, and 5% damped PSA for shallow crustal earthquakes. *Earthq Spectra* 30(3):1057–1085. <https://doi.org/10.1193/070113EQS184M>
- Bray JD, Rodriguez-Marek A (2004) Characterization of forward-directivity ground motions in the near-fault region. *Soil Dyn Earthq Eng* 24(11):815–828. <https://doi.org/10.1016/j.soildyn.2004.05.001>
- Building Seismic Safety Council (BSSC) (2001) NEHRP recommended provisions for seismic regulations for new buildings, and other structures, 2000 Edition. Part 1: provisions, building seismic safety council for the federal emergency management agency (Report FEMA368), Washington, DC
- Bulut F, Bohnhoff M, Eken T, Janssen C, Kılıç T, Dresen G (2012) The East Anatolian Fault Zone: Seismotectonic setting and spatiotemporal characteristics of seismicity based on precise earthquake locations. *J Geophys Res: Solid Earth*. <https://doi.org/10.1029/2011JB008966>
- Burks LS, Baker JW (2016) A predictive model for fling-step in near-fault ground motions based on recordings and simulations. *Soil Dyn Earthq Eng* 80:119–126. <https://doi.org/10.1016/j.soildyn.2015.10.010>
- CEN (2004) EN1998-1: Design of structures for earthquake resistance, Part 1: general rules, seismic actions and rules for buildings. European Committee for Standardization, Brussels
- Cetin KO, Ilgac M, Can G, Cakir E (2023) Preliminary reconnaissance report on the February 6, 2023, Pazarıcık Mw=7.7 and Elbistan Mw=7.6, Kahramanmaraş-Turkey earthquakes, Middle East Technical University Rept. No: METU/EERC 2023–01. <https://doi.org/10.13140/RG.2.2.15569.61283/1>
- Cetin KO, Kalkan E, Askan A, Bohnhoff M, Ergintav S, Konca AÖ, Taymaz T, Sabuncu YÇ, Gulerce Z (2024) Preface for the focus section on the 6 February 2023, Kahramanmaraş, Türkiye. *Earthq Seismol Res Lett* 95(2A):560–561. <https://doi.org/10.1785/0220240006>
- Champion C, Liel A (2012) The effect of near-fault directivity on building seismic collapse risk. *Earthq Eng Struct Dyn* 41:1391–1409. <https://doi.org/10.1002/eqe.1188>
- Cheloni D, Akinci A (2020) Source modelling and strong ground motion simulations for the 24 January 2020, Mw 6.8 Elazığ earthquake. *Turk Geophys J Int* 223(2):1054–1068. <https://doi.org/10.1093/gji/ggaa350>
- Cheloni D, Famiglietti NA, Akinci A, Caputo R, Vicari A (2024) Source modeling of the 2023 Mw 7.8 and 7.6 Türkiye earthquake sequence and implications for seismic potential along the Puturge fault from joint inversion of InSAR and GPS data, in preparation.
- Cheng Y, Mollaioli F, Donaire-Ávila J (2021) Characterization of dissipated energy demand. *Soil Dyn Earthq Eng* 147:106725. <https://doi.org/10.1016/j.soildyn.2021.106725>
- Chioccarelli E, Iervolino I (2010) Near-source seismic demand and pulse-like records: A discussion for L'Aquila earthquake. *Earthquake Eng Struct Dynam* 39(9):1039–1062. <https://doi.org/10.1002/eqe.987>


- Cork TG, Kim JH, Mavroeidis GP, Kim JK, Halldorsson B, Papageorgiou AS (2016) Effects of tectonic regime and soil conditions on the pulse period of near-fault ground motions. *Soil Dyn Earthq Eng* 80:102–118. <https://doi.org/10.1016/j.soildyn.2015.09.011>
- Delouis B, van den Ende M, Ampuero JP (2023) Kinematic rupture model of the 6 February 2023 Mw 7.8 Türkiye earthquake from a large set of near-source strong-motion records combined with GNSS offsets reveals intermittent supershear rupture. *Bull Seismol Soc Am* 113:1–15. <https://doi.org/10.1785/0120230077>
- Demir A, Celebi E, Ozturk H et al (2024) Destructive impact of successive high magnitude earthquakes occurred in Türkiye's Kahramanmaraş on February 6, 2023. *Bull Earthquake Eng*. <https://doi.org/10.1007/s10518-024-01865-5>
- Dindar AA, Yalçın C, Yüksel E, Özkaynak H, Büyükoztürk O (2015) Development of earthquake energy demand spectra. *Earthq Spectra* 31(3):1667–1689. <https://doi.org/10.1193/011212EQS010M>
- Ding H, Zhou Y, Ge Z, Taymaz T, Ghosh A, Xu H, Irmak TS, Song X (2023) High-resolution seismicity imaging and early aftershock migration of the 2023 Kahramanmaraş (SE Türkiye) M W 7.9 & 7.8 earthquake doublet. *Earthq Sci* 36(6):417–432. <https://doi.org/10.1016/j.eqs.2023.06.002>
- Duman TY, Emre Ö (2013) The East Anatolian Fault: geometry, segmentation and jog characteristics. *Geol Soc Lond Spec Publ* 372:495–529. <https://doi.org/10.1144/SP372.14>
- Ertuncay D, Costa G (2024) Analysis of impulsive ground motions from February 2023 Kahramanmaraş earthquake sequence. *Bull Earthq Eng*. <https://doi.org/10.1007/s10518-024-01897-x>
- Goldstein P, Snoko A (2005) SAC availability for the IRIS community, Incorporated Research Institutions for Seismology Newsletter, vol 7 (UCRL-JRNL-211140)
- Goldstein P, Dodge D, Firpo M, Minner L, Lee WHK, Kanamori H, Jennings PC, Kisslinger C (2003) SAC2000: Signal processing and analysis tools for seismologists and engineers. In: *The IASPEI International handbook of earthquake and engineering seismology*, vol 81, pp 1613–1620
- Goto H, Kaneko Y, Young J, Avery H, Damiano L (2019) Extreme accelerations during earthquakes caused by elastic flapping effect. *Sci Rep* 9(1):1117. <https://doi.org/10.1038/s41598-018-37716-y>
- Graizer V (2024) Application of GK17 ground-motion model to preliminary processed Turkish ground-motion recordings dataset and GK model adjustment to the Turkish environment by developing partially nonergodic model. *Seismol Res Lett* 95(2A):651–663. <https://doi.org/10.1785/0220230291>
- Grammatikou S, Fardis MN, Biskinis D (2022) Energy dissipation in reinforced concrete members before or after yielding. *Earthquake Eng Struct Dynam* 51(4):974–997. <https://doi.org/10.1002/eqe.3600>
- Gülerce Z, Askan A, Kale Ö, Sandıkkaya A, Işık NS, İlhan O, Can G, İlgaç M, Özacar AA, Çetin KÖ, Akbaş B, Altındal A, Sopaç E, Aydın MF, Güryuva B, Kanun O, Albayrak K, Muratoğlu G, Okçu OS, Aİçen(j) A, (2023) Preliminary reconnaissance report on February 6, 2023, Pazarçık Mw=7.7 and Elbistan Mw=7.6, Kahramanmaraş-Türkiye earthquakes: preliminary analysis of strong ground motion characteristics, Earthquake engineering research center, METU/EERC 2023–01.
- Hancılar U, Şeşetyan K, Çaktı E, Yenihayat N, Süleyman H, Açıkgöz N, Acar S (2023) Kahramanmaraş-Gaziantep Türkiye M7. 7 Earthquake, 6 February 2023 (04: 17 GMT+ 03: 00), Strong ground motion and building damage estimations preliminary report (v5)
- Hu J, Liu M, Taymaz T et al (2024) Characteristics of strong ground motion from the 2023 Mw 7.8 and Mw 7.6 Kahramanmaraş earthquake sequence. *Bull Earthquake Eng*. <https://doi.org/10.1007/s10518-023-01844-2>
- Hubert-Ferrari A, Lamair L, Hage S, Schmidt S, Çağatay MN, Avşar U (2020) A 3800 yr paleoseismic record (Lake Hazar sediments, eastern Turkey): implications for the East Anatolian Fault seismic cycle. *Earth Planet Sci Lett* 538:116152. <https://doi.org/10.1016/j.epsl.2020.116152>
- Iervolino I, Chioccarelli E, Baltzopoulos G (2012) Inelastic displacement ratio of near-source pulse-like ground motions. *Earthquake Eng Struct Dynam* 41(15):2351–2357. <https://doi.org/10.1002/eqe.2167>
- Jia Z et al (2023) The complex dynamics of the 2023 Kahramanmaraş, Turkey, Mw 7.8–7.7 earthquake doublet. *Science*. <https://doi.org/10.1126/science.adi0685>
- Kale Ö, Akkar S, Ansari A, Hamzehloo H (2015) A ground-motion predictive model for Iran and Turkey for horizontal PGA, PGV, and 5% damped response spectrum: Investigation of possible regional effects. *Bull Seismol Soc Am* 105(2A):963–980. <https://doi.org/10.1785/0120140134>
- Kalkan E, Kunnath SK (2006) Effects of fling step and forward directivity on seismic response of buildings. *Earthq Spectra* 22(2):367–390. <https://doi.org/10.1193/1.2192560>
- Karabacak A (2013) Evolution of the northern dead sea fault zone in southern Turkey. *J Geodyn* 65:282–291. <https://doi.org/10.1016/j.jog.2012.04.012>
- Mavroeidis GP, Papageorgiou AS (2010) Effect of fault rupture characteristics on near-fault strong ground motions. *Bull Seismol Soc Am* 100(1):37–58. <https://doi.org/10.1785/0120090018>
- McKenzie D (1972) Active tectonics of the Mediterranean region. *Geophys J Int* 30(2):109–185. <https://doi.org/10.1111/j.1365-246X.1972.tb02351.x>

- Melgar D, Taymaz T, Ganas A, Crowell B, Öcalan T, Kahraman M, Tsironi V, Yolsal-Çevikbilen S, Valkaniotis S, Irmak TS, Eken T, Erman C, Özkan B, Doğan AH, Altuntas C (2023) Sub- and super-shear ruptures during the 2023 Mw 7.8 and Mw 7.6 earthquake doublet in SE Türkiye. *Seismica*. <https://doi.org/10.26443/seismica.v2i3.387>
- Meng J, Kusky T, Mooney WD, Bozkurt E, Bodur MN, Wang L (2024) Surface deformations of the 6 February 2023 earthquake sequence, eastern Türkiye. *Science* 383(6680):298–305. <https://doi.org/10.1126/science.adj3770>
- Met Office. (2010–2015) Cartopy: a cartographic python library with a matplotlib interface. Retrieved from <https://scitools.org.uk/cartopy>.
- Ministry of Environment and Urbanization of Turkey (2023) <https://hasartespit.csb.gov.tr/>
- Nalbant SS, McCloskey J, Steacy S, Barka AA (2002) Stress accumulation and increased seismic risk in eastern Turkey. *Earth Planet Sci Lett* 195(3–4):291–298. [https://doi.org/10.1016/S0012-821X\(01\)00592-1](https://doi.org/10.1016/S0012-821X(01)00592-1)
- Okay HB, Özacar AA (2023) A Novel Prediction Strategy Taking Fluid Saturation into Account and a New Model of Türkiye. *Bull Seismol Soc Am* 114(2):1048–1065. <https://doi.org/10.1785/0120230032>
- Ozkula G, Dowell RK, Baser T, Lin JL, Numanoglu OA, İlhan O, Olgun CG, Huang CW, Uludag TD (2023) Field reconnaissance and observations from the February 6, 2023. *Turk Earthq Seq Nat Hazards*. <https://doi.org/10.1007/s11069-023-06143-2>
- Ragon T, Simons M, Bletley Q, Cavalie O, Fielding E (2021) A stochastic view of the 2020 Elazığ Mw 6.8 earthquake (Turkey). *Geophys Res Lett*. <https://doi.org/10.1029/2020GL090704>
- Reilinger R et al (2006) GPS constraints on continental deformation in the Africa-Arabia-Eurasia continental collision zone and implications for the dynamics of plate interactions. *J Geophys Res*. <https://doi.org/10.1029/2005JB004051>
- Reitman NG, Briggs RW., Barnhart WD, Thompson Jobe JA, DuRoss CB, Hatem AE, Gold RD, Akçiz S, Koehler RD, Mejstrik JD, Collett C (2023). Fault rupture mapping of the 6 February 2023 Kahramanmaraş, Türkiye, earthquake sequence from satellite data: U.S. geological survey data release, <https://doi.org/10.5066/P985I7U2>.
- Ren C, Wang Z, Taymaz T, Hu N, Luo H, Zhao Z, Yue H, Song X, Shen Z et al (2024) Supershear triggering and cascading fault ruptures of the 2023 Kahramanmaraş Türkiye, Earthquake doublet. *Science* 383:305–311. <https://doi.org/10.1126/science.adi1519>
- GRADE Report (2023) Global rapid post-disaster damage estimation (GRADE) Report February 6, 2023 Kahramanmaraş Earthquakes Türkiye Report.
- Rosakis A, Abdelmeguid M, Elbanna A (2023) Evidence of early supershear transition in the Mw 7.8 Kahramanmaraş earthquake from near-field records. arXiv preprint [arXiv:2302.07214](https://arxiv.org/abs/2302.07214). <https://doi.org/10.48550/arXiv.2302.07214>.
- Saroglu F, Emre O, Kuscü O (1992) The East Anatolian fault zone of Turkey. *Ann Tecton* 6:99–125
- Sheinarti MR, Darawcheh R, Mouty M (2005) The historical earthquakes of Syria: an analysis of large and moderate earthquakes from 1365 BC to 1900 AD. *Ann Geoph* 48(3):347–435
- Sesetyan K, Sakin O, Sönmez S, Tümsa MBD (2020) Seismic history of Central North Anatolian region: new contribution from Ottoman Archives. *Seismol Res Lett* 91(5):2590–2600. <https://doi.org/10.1785/0220200095>
- Sesetyan K, Demircioglu M, Rovida A, Albini P, Stucchi M (2013) SHARE-CET, the SHARE earthquake catalogue for Central and Eastern Turkey complementing the SHARE European Earthquake Catalogue (SHEEC). <http://www.emidius.eu/SHEEC>.
- Shahi SK, Baker JW (2014) An efficient algorithm to identify strong-velocity pulses in multicomponent ground motions. *Bull Seismol Soc Am* 104(5):2456–2466. <https://doi.org/10.1785/0120130191>
- Somerville PG, Smith NF, Graves RW, Abrahamson NA (1997) Modification of empirical strong ground motion attenuation relations to include the amplitude and duration effects of rupture directivity. *Seismol Res Lett* 68(1):199–222. <https://doi.org/10.1785/gssrl.68.1.199>
- Tatar O, Sözbilir H, Koçbulut F, Bozkurt E, Aksoy E, Eski S, Metin Y (2020) Surface deformations of 24 January 2020 Sivrice (Elazığ)–Doğanyol (Malatya) earthquake (Mw= 6.8) along the Pütürge segment of the East Anatolian Fault Zone and its comparison with Turkey’s 100-year-surface ruptures. *Mediterr Geosci Rev* 2:385–410. <https://doi.org/10.1007/s42990-020-00037-2>
- Taymaz T, Westaway R, Reilinger R (2004) Active faulting and crustal deformation in the Eastern Mediterranean Region. *Tectonophysics* 391(1–4):375. <https://doi.org/10.1016/j.tecto.2004.07.005>.
- Turkish Building Earthquake Code (TBEC) (2007) TC Ministry of Environment and Urbanization, Ankara.
- Türkiye Bina Deprem Yönetmeliği (TBDY) (2018) TC Başbakanlık Afet ve Acil Durum Yönetimi Başkanlığı, Deprem Dairesi Başkanlığı, <http://www.deprem.afad.gov.tr>.
- Ucar T, Mertes O (2024) Ductility demands for stiffness-degrading SDOF systems under pulse-like ground motions of the 2023 Pazarlık (Kahramanmaraş) earthquake. *Bull EarthqEng* 22:3243–3260. <https://doi.org/10.1007/s10518-024-01882-4>

- USGS (2023) M7.8 and M7.5 Kahramanmaraş Earthquake Sequence near Nurdagi, Turkey (Türkiye) available U.S. Geological Survey ([usgs.gov](https://www.usgs.gov))
- Vuran E, Serhatoğlu C, Timurağaoğlu MÖ, Smyrou E, Bal İE, Livaoglu R (2023) Damage observations of RC buildings from 2023 Kahramanmaraş earthquake sequence and discussion on the seismic code regulations. *Bull Earthq Eng*. <https://doi.org/10.1007/s10518-023-01843-3>
- Walters RJ, England PC, Houseman GA (2017) Constraints from GPS measurements on the dynamics of the zone of convergence between Arabia and Eurasia. *J Geophys Res: Solid Earth* 122(2):1470–1495. <https://doi.org/10.1002/2016JB013370>
- Wan Z, Dong R, Wang D, Xu S, Wang Z, Wang Q (2024) Along-strike variation of rupture characteristics and aftershock patterns of the 2023 mw 7.8 türkiye earthquake controlled by fault structure. *Seismol Res Lett*. <https://doi.org/10.1785/0220230378>
- Wang Z, Zhang W, Taymaz T, He Z, Xu T, Zhang Z (2023) Dynamic rupture process of the 2023 Mw 7.8 Kahramanmaraş earthquake (SE Türkiye): Variable rupture speed and implications for seismic hazard. *Geophys Res Lett* 50:e2023GL104787. <https://doi.org/10.1029/2023GL104787>
- Wessel P, Smith WH, Scharroo R, Luis J, Wobbe F (2013) Generic mapping tools improved version released. *Eos Trans AGU* 94(45):409–410
- Westaway R (2004) Kinematic consistency between the dead sea fault zone and the Neogene and quaternary left-lateral faulting in SE Turkey. *Tectonophysics* 391(1–4):203–237. <https://doi.org/10.1016/j.tecto.2004.07.014>
- Xie J, Zimmaro P, Li X, Wen Z (2017) Rupture directivity effects on strong ground motion during the 15 April 2016 MW 7.0 Kumamoto earthquake in Japan. *Bull Seismol Soc Am* 107(3):1265–1276. <https://doi.org/10.1785/0120160258>
- Yang H, Li Y, Hu L, Pan W, Ji S (2024) New baseline correction method for near-fault ground-motion records based on continuous wavelet transform. *Seismol Res Lett* 95(2A):607–625. <https://doi.org/10.1785/0220230184>

Publisher's Note Springer Nature remains neutral with regard to jurisdictional claims in published maps and institutional affiliations.

Authors and Affiliations

Aybige Akinci¹  · Ahmet Anil Dindar² · Ihsan E. Bal³ · Deniz Ertuncay^{4,5} · Eleni Smyrou³ · Daniele Cheloni¹

✉ Aybige Akinci
aybige.akinci@ingv.it

¹ Istituto Nazionale di Geofisica e Vulcanologia, Via di Vigna Murata 605, 00143 Rome, Italy

² Marmara Research and Training Center for Disaster Resilient Structures, Gebze Technical University, 41400 Kocaeli, Turkey

³ Research Centre for Built Environment NoorderRuimte, Hanze University of Applied Sciences Groningen, 9701 DA Groningen, The Netherlands

⁴ SeisRaM Working Group, Department of Mathematics, Informatics and Geosciences, University of Trieste, Via EduardoTurkey, Weiss 4, 34128 Trieste, Italy

⁵ Center for Seismological Research, National Institute of Oceanography and Applied Geophysics-OGS, Via Treviso, 55, 33100 Udine, Italy